

# SHELL EFFECTS IN NUCLEI WITH VECTOR SELF-COUPLING OF OMEGA MESON IN RELATIVISTIC HARTREE-BOGOLIUBOV THEORY

Madan M. Sharma, Ameenah R. Farhan and S. Mythili  
Physics Department, Kuwait University, Kuwait 13060

October 25, 2018

## Abstract

Shell effects in nuclei about the stability line are investigated within the framework of the Relativistic Hartree-Bogoliubov (RHB) theory with self-consistent finite-range pairing. Using 2-neutron separation energies of Ni and Sn isotopes, the role of  $\sigma$ - and  $\omega$ -meson couplings on the shell effects in nuclei is examined. It is observed that the existing successful nuclear forces (Lagrangian parameter sets) based upon the nonlinear scalar coupling of  $\sigma$ -meson exhibit shell effects which are stronger than suggested by the experimental data. We have introduced nonlinear vector self-coupling of  $\omega$ -meson in the RHB theory. It is shown that the inclusion of the vector self-coupling of  $\omega$ -meson in addition to the nonlinear scalar coupling of  $\sigma$ -meson provides a good agreement with the experimental data on shell effects in nuclei about the stability line. A comparison of the shell effects in the RHB theory is made with the Hartree-Fock Bogoliubov approach using the Skyrme force SkP. It is shown that the oft-discussed shell quenching with SkP is not consistent with the available experimental data.

# 1 Introduction

The Relativistic Mean-Field (RMF) theory [1] has proved to be successful in providing a framework for description of various facets of nuclear properties [2, 3, 4, 5, 6, 7]. In the RMF theory, the nuclear force is produced by a virtual exchange of various mesons. The nuclear saturation is achieved by a balance between an attractive  $\sigma$ - and a repulsive  $\omega$ -field. The relativistic Lorentz covariance of the theory allows an intrinsic spin-orbit interaction based upon exchange of  $\sigma$ - and  $\omega$ -mesons. This has been shown to be advantageous for properties which depend upon spin-orbit potential [8]. An immediate advantage of the proper spin-orbit potential has been the success [8] of the RMF theory to be able to describe the anomalous kink in the isotope shifts of Pb nuclei. The isotope shifts of Pb have been measured with a high precision using atomic beam laser spectroscopy [9] and are known to show a pronounced kink about the magic number  $N=126$ . The non-relativistic approaches based upon the Skyrme and Gogny forces have been unable to reproduce this kink [10]. It was shown [11] that this difference in the predictions of the Skyrme model and the RMF theory is due to the isospin dependence of the spin-orbit term. The Skyrme model assumes an isospin independent two-body spin-orbit force. A strong isospin dependence is, however, introduced herein by the exchange term. On the other hand, the isospin dependence in the RMF theory is provided mainly by the coupling constant  $g_\rho$  of the  $\rho$ -meson. However, as the strength of the spin-orbit term derives from a large sum of the absolute values of the scalar and vector fields, the  $\rho$ -field is rendered much weaker in comparison. Consequently, the isospin dependence of the spin-orbit potential in the RMF theory is relatively weak. A weak isospin dependence of the spin-orbit potential in the RMF theory was also concluded from calculations employing asymmetric semi-infinite nuclear matter [12].

The RMF theory has achieved significant success in respect of nuclei near the stability line as well as for nuclei far away from the stability line [3, 5, 6, 13]. The binding energies, charge radii, deformation properties and isotope shifts are some of the properties which

are described successfully in the RMF theory. The nonlinear scalar self-coupling of  $\sigma$ -meson has been the most successful model of the RMF theory used so far. With the need to describe highly exotic nuclei far away from the stability line, where the particles couple to the continuum, Relativistic Hartree-Bogoliubov (RHB) theory with a self-consistent pairing has been developed [14]. It has been shown [15, 16] that the RHB theory which uses the nonlinear scalar model provides a good description of nuclei away from the stability line. However, the level densities in the RMF or the RHB theory are perceived to be generally low, which lead to larger shell gaps. The large shell gaps imply that shell effects are stronger than in the experimental data. In the present work, we focus upon the shell effects and investigate the role of various meson couplings on the shell effects.

The shell effects manifest strongly in nuclei with magic particle numbers. Such an effect is well known to exist experimentally in many nuclei all over the periodic table, whereby a stronger binding is exhibited by these nuclei as compared to neighbouring nuclei. Nuclei with a particle or two above a magic number show a significantly reduced binding for the extraneous particles above the shell closure. The origin of shell closure has long been understood [17] due to spin-orbit coupling and to an ensuing splitting of levels. The spin-orbit potential and a bunching of levels create shell closures (magic numbers) which are predicted correctly by most of the models. In the non-relativistic density-dependent theory of the Skyrme type [18], the spin-orbit interaction is added phenomenologically and its strength is adjusted to reproduce the spin-orbit splitting in  $^{16}\text{O}$ . In the RMF theory, on the other hand, the spin-orbit interaction arises naturally due to exchange of  $\sigma$  and  $\omega$  mesons by the nucleons. The strength of the interaction is determined by the spin-orbit splitting in  $^{16}\text{O}$  and other nuclei, which is uniquely decided by the effective mass. This constrains an effective mass  $m^*$  in the vicinity of  $\sim 0.60$  in the RMF models [2].

The nature of the shell effects about the stability line is well established through the experimental data available on the binding energies and on one- and two-particle separation energies over a large region of the periodic table. The experimental data

encompass all the known magic numbers. Using the experimental binding energies on 2-neutron and 2-proton separation energies have been plotted in ref. [19] for nuclei all over the periodic table. An unambiguous kink appears in the separation energies across all the major magic numbers, demonstrating the existence of a major shell closure at these numbers. This also shows that the shell effects at most of the major magic numbers along the line of stability are strong.

It is not clear how the magic numbers or the shell closures behave in going to extreme regions of the periodic table such as near the drip lines. Experimental data about neutron drip-line in the region of light nuclei are gradually emerging [20, 21, 22, 23, 24]. As the neutron drip-line for medium-heavy and heavy nuclei is predicted to lie very far away (with abnormally large neutron excesses) from the stability line, it is not expected that experimental data on such nuclei would become available in the near future. However, information on shell effects in such nuclei in the vicinity of drip lines are vital to understanding the r-process nucleosynthesis of heavy nuclei [25]

Shell effects near the drip lines have been a matter of intense debate in the last few years. Within the framework of the RMF theory, it was shown that shell effects about  $N=82$  in the vicinity of the neutron drip-line remain strong [26]. These conclusions were based upon the RMF theory with the non-linear scalar potential of  $\sigma$ -meson. On the other hand, on the basis of the Hartree-Fock-Bogoliubov approach with the Skyrme interaction SkP, it was contended that the shell effects at  $N=82$  in the vicinity of the neutron drip-line show a strong quenching [27]. However, in the absence of any data in this region in foreseeable future, it is difficult to ascertain whether the shell effects near the drip-line remain strong or are quenched. Therefore, this debate needs to look into other observables or evidences which might support or refute the either contention. In this paper, we begin with our investigations of shell effects first along the stability line where experimental data is available. Having founded the basis, it could then be extended to predict behaviour of the shell effects at the drip lines. With this in mind, we include the nonlinear vector self-coupling of  $\omega$ -meson in the Lagrangian of the RMF theory.

The non-linear vector self-coupling of  $\omega$ -meson was introduced by Bodmer [28] and properties of nuclear matter were discussed on adding a quartic term in  $\omega$ -meson potential. The vector self-coupling to the properties of finite nuclei was applied in ref. [29]. It was noticed [28] that the inclusion of the vector self-coupling of  $\omega$  meson in addition to the non-linear scalar self-coupling of  $\sigma$  meson has the effect of softening the high-density equation of state (EOS) of the nuclear matter. The EOS of nuclear matter has been investigated [30] by taking expansion terms of higher orders in the  $\sigma$  and  $\omega$  fields. Recently, a comprehensive study of the vector self-coupling and its effect on properties of nuclei and nuclear matter has been undertaken [31]. An emphasis has been given to various facets of finite nuclei. It is shown [31] that an inclusion of the vector self-coupling of  $\omega$ -meson gives an improved description of nuclei as compared to the frequently used scalar self-coupling of  $\sigma$ -meson only. Two new forces NL-SV1 and NL-SV2 have been proposed [31] with a view to improve the predictions of the ground-state properties of nuclei. We will employ these forces in the present work. Details of this study will be provided elsewhere [31].

In this paper, we discuss the details of the RHB theory preceded by a short review of the RMF approach. The calculational details are provided in the section thereafter. The main objective of this work is to investigate the shell effects in nuclei about the stability line using the vector self-coupling of  $\omega$  meson and compare the results with those from the scalar self-coupling of  $\sigma$  meson. We have taken the isotopic chains of Ni and Sn nuclei for this purpose. Experimental binding energies of these nuclei are available over a large range. This allows us to examine the shell effects in nuclei in the known region using the various models. The shell effects about the magic neutron numbers  $N=28, 50$  and  $82$  are explored. The RMF+BCS results are compared with those of the RHB theory. The results on binding energies and two-neutron separation energies are presented and discussed in Section 5. The single-particle levels with various approaches are presented for a few nuclei, with a view to reinforce the results on the shell effects. The last section summarizes the main conclusions.

## 2 The Relativistic Mean-Field Theory

The RMF approach [1] is based upon the Lagrangian density which consists of fields due to the various mesons interacting with the nucleons. The mesons include the isoscalar scalar  $\sigma$ -meson, the isovector vector  $\omega$ -meson and the isovector vector  $\rho$ -meson. The Lagrangian density is given by:

$$\begin{aligned} \mathcal{L} = & \bar{\psi}(i\rlap{/}\partial - M)\psi + \frac{1}{2}\partial_\mu\sigma\partial^\mu\sigma - U(\sigma) - \frac{1}{4}\Omega_{\mu\nu}\Omega^{\mu\nu} + \\ & \frac{1}{2}m_\omega^2\omega_\mu\omega^\mu + \frac{1}{4}g_4(\omega_\mu\omega^\mu)^2 - \frac{1}{4}\mathbf{R}_{\mu\nu}\mathbf{R}^{\mu\nu} + \frac{1}{2}m_\rho^2\rho_\mu\rho^\mu - \frac{1}{4}F_{\mu\nu}F^{\mu\nu} \\ & g_\sigma\bar{\psi}\sigma\psi - g_\omega\bar{\psi}\boldsymbol{\gamma}\boldsymbol{\omega}\psi - g_\rho\bar{\psi}\boldsymbol{\gamma}\boldsymbol{\rho}\boldsymbol{\tau}\psi - e\bar{\psi}\mathbf{A}\psi \end{aligned} \quad (1)$$

The bold-faced letters indicate the vector quantities. Here  $M$ ,  $m_\sigma$ ,  $m_\omega$  and  $m_\rho$  denote the nucleon-, the  $\sigma$ -, the  $\omega$ - and the  $\rho$ -meson masses respectively, while  $g_\sigma$ ,  $g_\omega$ ,  $g_\rho$  and  $e^2/4\pi = 1/137$  are the corresponding coupling constants for the mesons and the photon, respectively.

The  $\sigma$  meson is assumed to move in a scalar potential of the form:

$$U(\sigma) = \frac{1}{2}m_\sigma^2\sigma^2 + \frac{1}{3}g_2\sigma^3 + \frac{1}{4}g_3\sigma^4. \quad (2)$$

This was introduced by Boguta and Bodmer [32] in order to make a substantial improvement in the surface properties of finite nuclei. This Ansatz for the  $\sigma$ -potential has since become a standard and necessary ingredient for description of the properties of finite nuclei. Recently, several variations of the non-linear  $\sigma$  and  $\omega$  fields have been proposed [33]. The new proposals for the form of the Lagrangian need to be investigated with a view to constrain the form in compliance with the properties of nuclear matter and finite nuclei.

Here we have incorporated the non-linear vector self-coupling of the  $\omega$ -meson, in addition to the non-linear scalar potential of Eq. (2). The coupling constant for the non-linear  $\omega$ -term is denoted by  $g_4$  in the Lagrangian (1). The vector self-coupling of the  $\omega$ -meson was first proposed in ref. [28] where properties of nuclear matter associated to this potential were also discussed. However, the coupling constant of the new Ansatz can be constrained appropriately only within the framework of finite nuclei. One such attempt

was made in ref. [29] where parameter sets TM1 and TM2 were obtained. We have now performed a comprehensive investigation of the properties of nuclear matter and finite nuclei associated with the vector self-coupling [31].

The field tensors of the vector mesons and of the electromagnetic field take the following form:

$$\begin{aligned}
\Omega^{\mu\nu} &= \partial^\mu \omega^\nu - \partial^\nu \omega^\mu \\
\mathbf{R}^{\mu\nu} &= \partial^\mu \boldsymbol{\rho}^\nu - \partial^\nu \boldsymbol{\rho}^\mu \\
F^{\mu\nu} &= \partial^\mu \mathbf{A}^\nu - \partial^\nu \mathbf{A}^\mu
\end{aligned} \tag{3}$$

The mean-field approximation constitutes the lowest order of the quantum field theory. Herein, the nucleons are assumed to move independently in the meson fields. The latter are replaced by their classical expectation values. The ground-state of the nucleus is described by a Slater determinant  $|\Phi\rangle$  of single-particle spinors  $\psi_i$  ( $i = 1, 2, \dots, A$ ). The stationary state solutions  $\psi_i$  are obtained from the coupled system of Dirac and Klein-Gordon equations. The variational principle leads to the Dirac equation:

$$\{-i\alpha\nabla + V(\mathbf{r}) + \beta[m^*]\} \psi_i = \epsilon_i \psi_i \tag{4}$$

where  $V(\mathbf{r})$  represents the *vector* potential:

$$V(\mathbf{r}) = g_\omega \omega_0(\mathbf{r}) + g_\rho \tau_3 \rho_0(\mathbf{r}) + e \frac{1 - \tau_3}{2} A_0(\mathbf{r}) \tag{5}$$

and  $S(\mathbf{r})$  is the *scalar* potential

$$S(\mathbf{r}) = g_\sigma \sigma(\mathbf{r}) \tag{6}$$

which defines the effective mass as:

$$m^*(\mathbf{r}) = m + S(\mathbf{r}) \tag{7}$$

The Klein-Gordon equations for the meson fields are time-independent inhomogeneous

equations with the nucleon densities as sources.

$$\begin{aligned}
\{-\Delta + m_\sigma^2\}\sigma(\mathbf{r}) &= -g_\sigma\rho_s(\mathbf{r}) - g_2\sigma^2(\mathbf{r}) - g_3\sigma^3(\mathbf{r}) \\
\{-\Delta + m_\omega^2\}\omega_0(\mathbf{r}) &= g_\omega\rho_v(\mathbf{r}) + g_4\omega^3(\mathbf{r}) \\
\{-\Delta + m_\rho^2\}\rho_0(\mathbf{r}) &= g_\rho\rho_3(\mathbf{r}) \\
-\Delta A_0(\mathbf{r}) &= e\rho_c(\mathbf{r})
\end{aligned} \tag{8}$$

For the case of an even-even nucleus with time-reversal symmetry, the spatial components of the vector fields,  $\boldsymbol{\omega}$ ,  $\boldsymbol{\rho}_3$  and  $A$  vanish. For the mean-field, the nucleon spinors provide the corresponding source terms:

$$\begin{aligned}
\rho_s &= \sum_{i=1}^A \bar{\psi}_i \psi_i \\
\rho_v &= \sum_{i=1}^A \psi_i^+ \psi_i \\
\rho_3 &= \sum_{p=1}^Z \psi_p^+ \psi_p - \sum_{n=1}^N \psi_n^+ \psi_n \\
\rho_c &= \sum_{p=1}^Z \psi_p^+ \psi_p
\end{aligned} \tag{9}$$

where the sums are taken over the valence nucleons only. Consequently, the ground-state of a nucleus is obtained by solving the coupled system of the Dirac and Klein-Gordon equations self-consistently. The solution of the Dirac equation is achieved by using the method of oscillator expansion [3]. In the RMF approach, the pairing is included within the BCS scheme, where the pairing gaps are calculated from the experimental masses of neighbouring nuclei.

### 3 The Relativistic Hartree-Bogoliubov Theory

Nuclei which are known to show strong pairing correlations can be treated appropriately within the framework of the RHB approach. This is especially important when the pairing correlations in the middle of a shell become important. However, the pairing correlations for nuclei 2 neutrons less or more than a magic number can be expected to be similar in

the RHB and the BCS approach. This is due to the reason that the pairing correlations in such nuclei are reduced to a minimal level.

The RHB approach becomes more important while dealing with nuclei far away from the stability line and in particular for nuclei in the vicinity of the drip lines, whereby the Fermi level is usually very near the continuum. The coupling between the bound states and the states in the continuum is taken into account in the RHB theory. Thus, the RHB is a preferred scheme over the BCS in such cases. This seems to be necessary because we consider Ni nuclei also about and above  $N=50$ , which are already far away from the stability line. Moreover, the Sn isotopes being open-shell nuclei are known to exhibit strong pairing correlations. Thus, we employ the RHB theory as being the most suitable one for the purpose.

Analogous to the Hartree-Fock-Bogoliubov (HFB) theory [34], the RHB theory contains the self-consistent field  $\hat{\Gamma}$  which represents the particle-hole correlations, and a pairing field  $\hat{\Delta}$  which includes all particle-particle correlations. For the self-consistent mean-field, the RHB equations are given by:

$$\begin{pmatrix} \hat{h}_D - m - \lambda & \hat{\Delta} \\ -\hat{\Delta}^* & -\hat{h}_D + m + \lambda \end{pmatrix} \begin{pmatrix} U_k(\mathbf{r}) \\ V_k(\mathbf{r}) \end{pmatrix} = E_k \begin{pmatrix} U_k(\mathbf{r}) \\ V_k(\mathbf{r}) \end{pmatrix}. \quad (10)$$

where  $\hat{h}_D$  is the single-nucleon Dirac Hamiltonian and  $m$  is the nucleon mass.  $U_k$  and  $V_k$  are the two Dirac spinors and  $\hat{\Delta}$  represents the pairing field. These equations are solved self-consistently, whereby the potentials are obtained in the mean-field approximation from the Klein-Gordon equations (8).

The corresponding source terms in the Klein-Gordon equations are sums of bilinear products of baryon amplitudes

$$\rho_s(\mathbf{r}) = \sum_{E_k > 0} V_k^\dagger(\mathbf{r}) \gamma^0 V_k(\mathbf{r}), \quad (11)$$

$$\rho_v(\mathbf{r}) = \sum_{E_k > 0} V_k^\dagger(\mathbf{r}) V_k(\mathbf{r}), \quad (12)$$

$$\rho_3(\mathbf{r}) = \sum_{E_k > 0} V_k^\dagger(\mathbf{r}) \tau_3 V_k(\mathbf{r}), \quad (13)$$

$$\rho_{\text{em}}(\mathbf{r}) = \sum_{E_k > 0} V_k^\dagger(\mathbf{r}) \frac{1 - \tau_3}{2} V_k(\mathbf{r}), \quad (14)$$

where the sums are taken over all positive energy states. For  $M$  degrees of freedom, one chooses the  $M$  positive eigenvalues  $E_k$  for the solution that corresponds to a ground state of a nucleus with an even particle number. The negative energy solutions are ignored as it is forbidden to occupy the levels  $E_k$  and  $-E_k$  simultaneously.

The integral operator  $\hat{\Delta}$  in eq. (10) acts on the wave function  $V_k(\mathbf{r})$ :

$$(\hat{\Delta}V_k)(\mathbf{r}) = \sum_b \int d^3r' \Delta_{ab}(\mathbf{r}, \mathbf{r}') V_{bk}(\mathbf{r}'). \quad (15)$$

For the pairing field, the kernel of the integral operator is given by

$$\Delta_{ab}(\mathbf{r}, \mathbf{r}') = \frac{1}{2} \sum_{c,d} V_{abcd}(\mathbf{r}, \mathbf{r}') \kappa_{cd}(\mathbf{r}, \mathbf{r}'). \quad (16)$$

where  $a, b, c, d$  denote all quantum numbers, except the coordinate  $\mathbf{r}$ , that specify the single-nucleon states. Here  $V_{abcd}(\mathbf{r}, \mathbf{r}')$  denotes matrix elements of a general two-body pairing interaction, and

$$\kappa_{cd}(\mathbf{r}, \mathbf{r}') = \sum_{E_k > 0} U_{ck}^*(\mathbf{r}) V_{dk}(\mathbf{r}'). \quad (17)$$

is the pairing tensor.

The system of the Dirac-Hartree-Bogoliubov equations (10-17) is solved self-consistently. The eigensolutions of the RHB equations (10) form a set of orthonormal single quasi-particle states and the corresponding eigenvalues are the single quasi-particle energies. The basis of the quasi-particles is then transformed into the canonical basis of the single-particle states. This basis determines the single-particle energies and occupations probabilities corresponding to the ground-state of a nucleus.

It was realized earlier that using the standard parameter sets of the RMF theory for the pairing, one obtains highly unrealistic pairing correlations [35]. Due to this reason, a completely microscopic derivation of a pairing interaction from the first principles has not been feasible so far. Instead, the finite-range pairing force of the Gogny-type is used in the p-p channel as suggested in ref. [14]. The pairing interaction is approximated by a

two-body finite range force of the Gogny type,

$$V^{pp}(1, 2) = \sum_{i=1,2} e^{-((\mathbf{r}_1-\mathbf{r}_2)/\mu_i)^2} (W_i + B_i P^\sigma - H_i P^\tau - M_i P^\sigma P^\tau), \quad (18)$$

with parameters  $\mu_i$ ,  $W_i$ ,  $B_i$ ,  $H_i$  and  $M_i$  ( $i = 1, 2$ ). We use the parameter set D1S [36] for the pairing force. The Gogny force is a sum of two Gaussians with finite range. It has been shown [36] that the Gogny force is able to represent the pairing properties of a large number of finite nuclei including the Sn and Pb isotopes.

## 4 Details of the Calculations

We have performed the RMF+BCS and RHB calculations for Ni and Sn nuclei with a spherical symmetry. For both the RMF+BCS and RHB calculations, the wavefunctions are expanded into the oscillator basis. The number of shells taken into account is 20 for the fermionic as well as bosonic wavefunctions.

In this study, we have used the forces NL-SH and NL3 for the Lagrangian with the non-linear scalar self-coupling. In a large number of studies it has been shown that the force NL-SH [5] is able to provide a very good description of the ground-state properties of nuclei all over the periodic table. It has been found to be especially useful for exotic nuclei near drip lines. Recently, the force NL3 [37] has been proposed with a view to modify the compression modulus of nuclear matter. Studies have shown [38] that the force NL3 describes the ground-state properties of nuclei as well as NL-SH and that NL3 results are found to be very similar to the NL-SH ones.

We have also used the forces NL-SV1 and NL-SV2 [31] for the Lagrangian with the scalar and vector self-coupling. The most important point in the development of the forces NL-SV1 and NL-SV2 is to soften the equation of state (EOS) for the nuclear matter as compared to that with the scalar self-coupling only and to improve the description of the ground-state properties of nuclei vis-a-vis the forces with the scalar self-coupling. We have also used the force TM1 [29] for a comparative view of the results.

## 5 Results and Discussion

We have chosen the chain of Ni and Sn isotopes for the present study. The Ni isotopes are known to be spherical in the neighbourhood of the stability line and this trend continues well up to the neutron shell closure  $N=50$ . The Ni isotopes are favourable for the study of shell effects, as the shells in these nuclei are spread broadly. The large shells gaps are conducive to exploring the shell effects. The effects due to the large shell gaps appear more prominently in the experimental observables such as 2-neutron separation energies. This is exemplified by a large value of about 32 MeV of the 2-neutron separation energy,  $S_{2n}$ , for the nucleus  $^{56}\text{Ni}$ . With the addition of a pair of neutrons to form  $^{58}\text{Ni}$ , the  $S_{2n}$  value shows a dramatic decrease to  $\sim 22$  MeV in the experimental value. This large difference in  $S_{2n}$  values of the Ni isotopes should serve as a good test-bench to examine the shell effects.

For heavier mass nuclei such as Sn isotopes, the shells become compressed and consequently the  $S_{2n}$  values show a lesser sensitivity to the shell effects. In the present case, we examine the shell effects in Sn nuclei at  $N=82$ . The experimental binding energies of the neutron-rich nuclei  $^{132}\text{Sn}$ ,  $^{134}\text{Sn}$  and  $^{136}\text{Sn}$  are available. This makes it possible to look into the shell effects at  $N=82$  in Sn nuclei away from the stability line.

### 5.1 Ni Isotopes

#### 5.1.1 Binding Energies

We show the binding energies of the Ni isotopes with the forces in the non-linear scalar coupling of the  $\sigma$ -meson. The binding energies ( $B_{th}$ ) of the Ni isotopes as compared to the experimental values ( $B_{exp}$ ) [39] are shown in Fig. 1. The results of the RMF theory (Fig. 1a) with the BCS pairing are compared to those with Relativistic Hartree-Bogoliubov (RHB) approach using the self-consistent finite-range pairing (Fig. 1b). For the BCS calculations, the proton number  $Z=28$  is assumed to be a closed shell and hence the proton pairing gap is taken to be zero. The neutron pairing gap is calculated using the experimental binding energies of neighbouring nuclei. However, for the magic nuclei with

N=28 and N=50, the neutron pairing gap is taken to be zero.

The results in Fig. 1a show that the RMF+BCS approach reproduces the binding energies of the most of the Ni isotopes well. Only for a few nuclei about A=62 (N=34), the RMF theory underestimates the binding energy by about 3-4 MeV ( $\sim 0.5\%$ ). A comparison of the results of NL-SH and NL3 shows that the binding energies with NL3 are similar to those of NL-SH and that both the forces show a similar pattern of behaviour. The binding energies with NL-SH are slightly better than those with NL3, especially in the region A=50-60.

The RHB results with the forces NL-SH and NL3 are shown in Fig. 1b. It can be seen that the RHB approach with the self-consistent pairing produces results which are very similar to those with the RMF+BCS ones. The whole pattern of the BCS+RMF results is reproduced by the RHB, with both the forces NL-SH and NL3. Moreover, the RHB results show an improved agreement for nuclei in the region A=62. A comparison of the results with NL-SH and NL3 shows that both the results are very similar to each other. For the region A=70-78, both the forces overestimate the experimental binding energies slightly in the RHB approach.

With the non-linear vector self-coupling of the  $\omega$ -meson, we have used the forces NL-SV1 and NL-SV2 [31]. We have also included the force TM1 [29]. The binding energy difference ( $B_{th} - B_{exp}$ ) is shown for the RMF+BCS (Fig. 2a) and the RHB approach (Fig. 2b) for the three forces. For the BCS pairing we have used the experimental pairing gaps obtained from the masses of neighbouring nuclei as mentioned above. The results (Fig. 2a) show that the behaviour of the binding energies with the forces with the scalar-vector self-coupling is similar to those with the scalar self-coupling only, except for a few minor differences. The region about A=60 shows some deviations from the experimental values. However, the degree of agreement with the experimental data varies with the forces. The force TM1 underestimates the binding energies by about 4 MeV for several nuclei in the region A=54-62. The force NL-SV1 shows an improvement in the predictions of energies of these nuclei over those of TM1. In comparison, the force NL-SV2 provides the best

description of the binding energies, where the deviations from the experimental energies are reduced considerably. For the heavier Ni isotopes with  $A=68-78$ , the results of NL-SV1 and NL-SV2 are very similar, whereas for TM1 deviations from the experimental energies start increasing at  $A=74$ .

We have incorporated the vector self-coupling of the  $\omega$ -meson in the RHB approach for the first time. The RHB results (Fig. 2b) with the forces with the scalar-vector self-coupling show a high degree of similarity with the corresponding BCS results, as seen also for the non-linear scalar coupling. Only a slight improvement is noticed in the RHB predictions. With the force NL-SV2 the deviations from the experimental binding energies are improved slightly in the RHB over the BCS for the region  $A=52-64$ . For the heavier isotopes, RHB shows marginally higher deviations than in the BCS with NL-SV2. The trend of the binding energies as a function of the mass number is smoothed in the RHB.

The RMF+BCS and RHB results of Figs. 1 and 2 demonstrate that the BCS results are able to mock the RHB results provided experimental pairing gaps are used. Secondly, the scalar-vector self-coupling force NL-SV2 provides a description of the binding energies which is considerably improved over that with the non-linear scalar self-coupling only.

### 5.1.2 Two-Neutron Separation Energies

The 2-neutron separation energies have been tabulated and plotted [19] over the whole periodic table using the experimental masses of nuclei. The salient feature in the curves of  $S_{2n}$  values in ref. [19] is a kink which can be observed conspicuously about all the major magic numbers. A kink implies that  $S_{2n}$  values for nuclei with 2 neutron numbers above a magic number exhibit a dramatic decrease as compared to a nucleus with the magic number or nuclei below the magic number. This sudden decrease in the  $S_{2n}$  values signifies a shell gap above the magic number and thus reflects the role played by the ensuing shell effects. The magnitude of a shell gap does also show a significant dependence on mass number of a nucleus. It is thus expected that the shell effects vary strongly depending upon the part of the periodic table one is considering.

Figure 3 shows the results obtained with the forces with the non-linear scalar self-coupling NL-SH (Fig. 3a) and NL3 (Fig. 3b). The results for the RMF+BCS and the RHB are compared with the experimental  $S_{2n}$  values (solid circles). A staggeringly high value of  $\sim 35.0$  MeV for the 2-neutron separation energy for the nucleus  $^{52}\text{Ni}$  can be seen. It decreases smoothly to 30.8 MeV for the doubly magic nucleus  $^{56}\text{Ni}$ . However, on adding 2-neutrons to the magic core, the  $S_{2n}$  value shows a dramatic decrease to 22.5 MeV for  $^{58}\text{Ni}$ . This difference in the  $S_{2n}$  values is a clear measure of the shell gap at the magic number. Inevitably, the downward kink at  $N=28$  provides a sensitive observable for an investigation of the shell effects in nuclei. Therefore, we focus upon the 2-neutron separation energies to analyze the characteristics of the shell effects.

A comparison of the BCS results with the RHB in Fig. 3 shows that except for a few minor differences, the two approaches provide results which are very close to each other for most of the isotopic chain. This is also the case in the extremely neutron-rich region. Essentially, these results mirror the accord in the binding energies in the two approaches as shown in Fig. 1. This implies that the experimental pairing gaps used in the BCS approach are adequately represented by the self-consistent Gogny pairing in the RHB approach.

For a comparative look at the various predictions,  $S_{2n}$  values for RMF+BCS are shown in Fig. 4a and for RHB in Fig. 4b. A striking similarity is observed in the results of Fig. 4a and Fig. 4b. It arises naturally due to the similarity in the predictions of the binding energies with RMF+BCS and RHB as already observed in Fig. 1. There are, however, two differences in the RHB results as compared to the BCS ones. Firstly, the inclusion of the self-consistent pairing in RHB increases the kink at  $N=28$  slightly. Secondly, the RHB results show an improved agreement with the experimental data in the region  $A=64-70$  as compared to the BCS results.

The RHB results employ the self-consistent pairing and ought to be considered as more realistic than BCS. Therefore, we focus our attention primarily upon the RHB results. As observed for the binding energies in Fig. 1, the  $S_{2n}$  values with RHB for NL-SH and

NL3 are also close to each other. As far as the experimental data is concerned, the RHB is able to describe the  $S_{2n}$  data on the lighter ( $A=52-56$ ) Ni isotopes very well. However, for nuclei just above the magic number  $N=28$ , i.e., for  $^{58}\text{Ni}$  and  $^{60}\text{Ni}$ , the RHB values are lower than the experimental values by about 2-2.5 MeV. This implies that the shell gap at  $N=28$  is higher in the theory than indicated by the experimental data. Thus, the RMF theory with the non-linear scalar coupling shows shell effects which are stronger than suggested by the experimental data.

It can be seen from Fig. 4b that for nuclei heavier than  $^{62}\text{Ni}$ , the  $S_{2n}$  values for NL-SH are closer to the experimental data than the NL3 values. The  $S_{2n}$  values for nuclei with  $A=70-78$  are reproduced successfully both by NL-SH and NL3. It may be noted that the empirical data on  $S_{2n}$  exist only up to  $^{78}\text{Ni}$ . The mass of the nucleus  $^{80}\text{Ni}$  is not known experimentally. Therefore, our knowledge about the shell effects far away from the stability line is severely constrained. In this context, the nucleus  $^{80}\text{Ni}$  constitutes one such nucleus which has a potential to expose shell effects in reaching out to the neutron drip-line. A measurement of the mass of the nucleus  $^{80}\text{Ni}$  would undoubtedly shed light on how the shell effects behave far away from the stability line. Here, we provide our predictions only on this account.

Due to uncertainties of pairing and coupling of states to the continuum, the BCS results are not expected to be fully realistic in this region. The RHB approach is the most appropriate one for the highly exotic Ni nuclei. The presence of a kink in the RHB results (Fig. 4b) at  $N=50$  signifies the existence of shell effects which are still strong far away from the stability line. Comparatively, the shell effects with NL-SH are slightly stronger than with NL3 in the extreme region. We will also compare the shell effects in the RHB approach to those in the Hartree-Fock Bogoliubov (HFB) approach with the Skyrme force SkP in the latter part of this paper.

The results on 2-neutron separation energy for the model with the scalar-vector self-coupling are presented in Fig. 5. Here we show the results with the forces NL-SV2 and TM1. The upper panel (Fig. 5a) displays the  $S_{2n}$  values with the BCS pairing. A com-

parison of the BCS results with the RHB results (Fig. 5b) in the region of experimentally known nuclei shows that the two approaches give results which are remarkably similar, provided the experimental pairing gaps are used in the BCS calculations.

Again, we focus upon the RHB results due to the self-consistency of the pairing. The results with NL-SV2 show a good agreement with the experimental data for most of the isotopic chain. For the region below  $N=28$ , the  $S_{2n}$  values with NL-SV2 are closer to the experimental data than those with TM1. The relative difference in the  $S_{2n}$  values of nuclei  $^{56}\text{Ni}$  and  $^{58}\text{Ni}$  with TM1 is less than the experimental data, whereas it is closer to the experimental difference for the force NL-SV2. In the region  $A=62-68$ , where deviations from the experimental data are most notable, the NL-SV2 results are closer to the experimental data than TM1. This is due to a better degree of agreement with the experimental binding energies obtained by using the vector self-coupling force NL-SV2 as shown in Fig. 2.

### 5.1.3 Shell Effects

We compare in Fig. 6 the  $S_{2n}$  values obtained with the scalar-self coupling (NL-SH) to those with the scalar-vector self-coupling (NL-SV2). In Fig. 6a the  $S_{2n}$  values across the shell-closure  $N=28$  are presented. A comparison with the experimental data about  $N=28$  shows that the force NL-SH gives shell effects which are stronger than suggested by the empirical data. The relative difference between the  $S_{2n}$  values of  $^{56}\text{Ni}$  and  $^{58}\text{Ni}$  is 11.1 MeV with NL-SH and 9.2 MeV with NL-SV2. The difference in the  $S_{2n}$  values of nuclei about a shell closure is an indicator of the shell gap at the magic number. The results show that the shell gap at  $N=28$  is reduced considerably with the scalar-vector self-coupling (NL-SV2) as compared to the scalar coupling. In comparison, the experimental difference amounts to about 8.4 MeV. Thus, the shell gap at  $N=28$  with NL-SV2 is very close to the experimental one.

Shell effects with the Hartree-Fock Bogoliubov approach using the Skyrme force SkP have been discussed often in the literature [40, 41, 42]. In order to clarify the situation,

we include the  $S_{2n}$  values [43] obtained in the HFB approach with the force SkP in Fig. 6a. It is seen clearly that the SkP values cross the shell-closure N=28 (A=56) smoothly. This has an unambiguous implication that *contrary* to the experimental observation, the shell effects with SkP are quenched strongly at N=28 and consequently the shell gap at N=28 is diminished considerably. This aspect of SkP will become obvious in the following where we compare single-particle levels from various approaches.

The 2-neutron separation energies across the N=50 shell closure are shown in Fig. 6b. The experimental data on  $S_{2n}$  is available only up to A=78 (N=50) as shown by the solid circles. How the shell effects behave about N=50 in the region very far away from the stability line is still an open question ? We will show elsewhere [44] that the very few experimental data available for N=50 are consistent with strong shell effects. Determination of the nature of shell effects for waiting-point nuclei in the vicinity of N=50 are crucial to understanding the r-process nucleosynthesis in the neighbourhood of A=80. A future measurement of mass of the nucleus  $^{80}\text{Ni}$  would help resolve this issue. In the present work, we make our predictions on the basis of the extrapolation from the region of stability. A comparison of the  $S_{2n}$  values for  $^{78}\text{Ni}$  (N=50) and  $^{80}\text{Ni}$  for the forces NL-SH and NL-SV2 show that the shell gap at N=50 is larger for NL-SH than for NL-SV2. This situation is very similar to that we have seen in the known region of N=28. Thus, also at N=50 the shell effects with NL-SH are stronger than NL-SV2. Taking into account a good agreement of NL-SV2 results with the experimental data about N=28, we predict that at N=50 the shell effects still remain strong. This is in accordance with a general perception that the magic number N=50 constitutes a strong shell closure. This feature is thus predicted to persist also far away from the stability line. These results are contrasted sharply (Fig. 6b) with the results of the HFB with the Skyrme force SkP which predicts a smooth decrease in the  $S_{2n}$  values across the magic number N=50. The strong quenching of the shell effects at N=50 with SkP as seen here is consistent with the similar quenching shown by this force also at N=28 (see Fig. 6a).

#### 5.1.4 Single-Particle Levels

Differences in the shell effects in various approaches are exhibited succinctly in the single-particle spectrum as shown in Fig. 7. The neutron single-particle spectra for the nucleus  $^{58}\text{Ni}$  are displayed for the forces NL-SH and NL-SV2 and a comparison is made with SkP. The force NL-SV2 with the scalar-vector self-coupling shows a decrease in the shell gap at  $N=28$  as compared to NL-SH indicating again that the shell effects with NL-SV2 are softer. This is in conformity with the corresponding  $S_{2n}$  values in Fig. 6a.

The single-particle spectrum with SkP in Fig. 7 reveals a striking difference with that of NL-SH and NL-SV2. The levels with SkP are compressed significantly as compared to NL-SH and NL-SV2. The mean-field potential with SkP appears to be much shallower than the corresponding one in the RMF theory. The most important difference about the shell effects is that with SkP the shell gap at  $N=28$  is reduced significantly. This is the reason that a strong quenching of the shell effects is exhibited by SkP at  $N=28$ .

With a view to illustrate the shell effects at  $N=50$ , the single-particle levels for the nucleus  $^{80}\text{Ni}$  are shown in Fig. 8 for NL-SH, NL-SV2 and SkP. The shell gap at  $N=50$  with NL-SV2 is reduced as compared to that with NL-SH. This reduction in shell gap is similar to that also observed for  $N=28$  with NL-SV2 in Fig. 7. Thus, the behaviour of the single-particle levels for  $^{58}\text{Ni}$  and  $^{80}\text{Ni}$  and the reduced shell gaps at  $N=28$  and  $N=50$  serve to illustrate the point that the slightly-softer shell effects with NL-SV2 are consistent with the experimental data.

The single-particle spectrum for  $^{80}\text{Ni}$  with SkP in Fig. 8 is strikingly different than that for NL-SH and NL-SV2. The levels with SkP are compressed significantly as compared to NL-SH and NL-SV2. This feature is very similar to that portrayed in Fig. 7. In fact, such a feature seems to be a generic one for SkP. The single-particle spectrum for SkP shows that the shell gap at  $N=50$  with SkP is about a factor of 2 smaller than the corresponding one with NL-SV2. Therefore, with SkP the shell closure  $N=50$  is quenched strongly. This is consistent with the smooth decrease of  $S_{2n}$  values with SkP across  $N=50$  (see Fig. 6b).

The strikingly different single-particle scheme with SkP may be attributed to the ef-

fective mass  $m^* = 1$  assumed for this force. The effective mass has an important influence on the single-particle structure of nuclei. The quantities which lend their influence to a single-particle scheme are the effective mass and the compressibility of nuclear matter. The latter is intricately connected to the saturation density through the properties of finite nuclei. Recently, it has been shown that in the density dependent Skyrme approach, the shell effects show a significant dependence on the compressibility of nuclear matter [45].

In Fig. 9 we examine predictions on the shell effects from various mass models. The  $S_{2n}$  values are shown for the mass formulae the Finite-Range Droplet Model (FRDM) [46] and the Extended Thomas-Fermi with Strutinsky Integral (ETF-SI) [47]. The FRDM data about N=28 (Fig. 9a) are in close agreement with the experimental data, showing that the shell effects about N=28 are represented adequately in the FRDM. On the other hand, in the ETF-SI which is based upon the Skyrme Ansatz, the shell effects are weakened significantly at N=28. A comparison of the ETF-SI data with the SkP predictions shows that in both the cases, the shell effects are quenched strongly. It may be recalled that in the ETF-SI approach, shell corrections to a smooth component of energy-functional are added using the Strutinsky method. Thus, the nature of the shell corrections as obtained in this approach is crucial to deciding the strength of the shell effects.

At N=50 (Fig. 9b) predictions of the ETF-SI for the shell effects are, however, in stark contrast to those of SkP. Whilst SkP predicts a washing out of the shell effects at N=50 as discussed above, the ETF-SI, on the other hand, shows shell effects which are strong at N=50. This difference between ETF-SI and SkP at N=50 is not easy to understand notwithstanding the similar quenching at N=28 in both the approaches. The strength of the shell effects with SkP derives from the high value of the effective mass. This tends to reduce shell gaps at most of the magic numbers. On the other hand, shell effects in ETF-SI stem from as to how the shell effects are evaluated in different regions. Shell corrections in the ETF-SI based upon the experimental data in the region maintain a strong shell closure at N=50. A point of comparison, however, may be made here that

the magnitude of the shell gap as reflected by the  $S_{2n}$  values at  $N=50$  in ETF-SI is similar to that projected by the force NL-SV2. The FRDM results, however, show shell effects which are stronger than those predicted by both ETF-SI and NL-SV2.

## 5.2 Sn Isotopes

The Sn isotopes provide a very long chain where the experimental masses are known over a large range of isospin. The experimental data is presently available above the neutron magic number  $N=82$  up to the mass  $A=136$  ( $N=86$ ). This allows us to examine the shell effects about the neutron shell closure  $N=82$  which in the present case lies reasonably away from the stability line. The nature of the shell effects about  $N=82$  should reveal as to how the shell closure  $N=82$  retains (or loses) its magic character in the region far away from the stability line.

We have included Sn isotopes with mass  $A=100-138$  for the present study. It must be pointed out that the Sn isotopes have long been known to possess strong pairing properties akin to superfluidity. Thus, the role of the pairing is very important for the Sn nuclei. As in case of the Ni isotopes, we have performed RMF+BCS calculations using the pairing gap obtained from the experimental masses of neighbouring nuclei. We have also performed the RHB calculations using the self-consistent finite-range pairing.

### 5.2.1 Binding Energies

The binding energy differences ( $B_{th} - B_{expt}$ ) obtained with the two approaches are shown in Fig. 10. A direct comparison is made between the results of the forces NL-SH and NL3. The RMF+BCS results (Fig. 10a) show strong deviations from the experimental binding energies in the vicinity of  $A=100$ . For the other regions of the range, the NL-SH results are generally better than NL3. However, in the vicinity of the magic number  $N=82$  ( $A=132$ ), NL3 predictions are slightly better than those of NL-SH. The BCS results show several undulations which arise from the inadequacy of the BCS pairing. A kink due to the similar reasons is seen at  $A=108$  with both the forces.

The RHB results with the self-consistent pairing (Fig. 10b) are free from the fluctuations of Fig. 10a. The binding energies show a smooth trend with mass number and the kink at  $A=108$  has disappeared. The smoothness of the RHB results vis-a-vis the BCS ones is an indication that the self-consistent pairing is very important for nuclei like Sn isotopes.

The RHB results (Fig. 10b) with NL-SH and NL3 follow a similar pattern in the binding energy. It is observed that for the light Sn isotopes, NL-SH overestimates the binding energies by a few MeV. This aspect is especially apparent at the doubly magic nucleus  $A=100$  both for NL-SH and NL3. In the region  $A=100-110$ , the NL3 values show a better agreement with the experimental data than NL-SH. However, in the latter part of the chain where stable Sn isotopes exist, the NL-SH and NL3 results are very similar, showing a good agreement with the experimental data within 1-2 MeV. In the neighbourhood of  $A=132$  disagreement of about 2-3 MeV with the experimental data appear for both NL-SH and NL3.

For a direct comparison of the RMF+BCS with the RHB, we show in Fig. 11 the results from the two approaches for the forces NL-SH (a) and NL3 (b). The RHB results show a smooth behaviour with the mass number for both the forces. The change from BCS to RHB is moderate for NL-SH. However, for NL3 results the change from BCS values to the RHB values is much larger than NL-SH. Thus, the self-consistent pairing brings about a significant change in the energies of NL3 especially in the light-mass Sn nuclei. This shows that with the force NL3, the experimental pairing gaps are not able to take into account the pairing correlations correctly for the Sn nuclei in particular those with lower mass. On the whole, this situation of Sn isotopes is unlike the results of Ni isotopes (see Figs. 1 and 2) where the RHB results mirrored much the results from the BCS. In other words, within the BCS the experimental pairing gaps for the Ni isotopes were adequate to represent the pairing correlations.

In Fig. 12 we show the results with the forces with the scalar-vector self-couplings, with both the RMF+BCS and the RHB theory. Here the forces NL-SV1, NL-SV2 and

TM1 are included. The presence of a kink at  $A=108$  in the BCS calculations indicates that in spite of taking the pairing gaps from the experimental data, there seems to be an inconsistency in representing the pairing correlations appropriately in the BCS formalism. The smoothness of the RHB results with the self-consistent pairing shows that this drawback is eliminated in the RHB approach. This is true for all the forces included here. Examining the the BCS results only, it is seen that the binding energies with NL-SV1 and TM1 are closer to the experimental data than NL-SV2 for the light-mass Sn nuclei. NL-SV2 results in this region overpredict the experimental data slightly. For the region  $A=110-130$  the binding energies with all the forces show a good agreement with the data within about 1 MeV. In general, the BCS results with NL-SV1 show an overall good agreement with the data, except about the doubly magic nucleus  $^{100}\text{Sn}$ . In comparison, the TM1 results show a slightly higher disagreement with the data. The divergence of TM1 with the data is, however, more pronounced in the extreme region about  $A=136$ .

We have compared the RHB results with the scalar-vector self-coupling forces in Fig. 13. It is seen that the results of NL-SV2 and TM1 are similar over most of the mass range except in the vicinity of the doubly magic nucleus  $^{100}\text{Sn}$ . Both the forces overestimate the binding energies of Sn nuclei by about 2-4 MeV. This implies that the underlying pairing correlations with the given pairing force D1S are stronger for the forces NL-SV2 and TM1. On the other hand, the force NL-SV1 shows the best agreement with most of the data. The NL-SV1 results are within 1-2 MeV of the experimental energies except for the region about  $^{100}\text{Sn}$ . In the neighbourhood of the other doubly magic nucleus  $^{132}\text{Sn}$ , the NL-SV1 results are similar to NL-SV2 and are in agreement with the data within about 1-2 MeV.

### 5.2.2 Two-Neutron Separation Energies

The 2-neutron separation energies for the Sn isotopes with the RHB approach using the forces with the non-linear scalar self-coupling are shown in Fig. 14. For both the forces NL-SH and NL3, there is a very good agreement of the results with the experimental

data in the mass region  $A=110-132$ . Both the forces show a slight divergence from the experimental values as one moves below  $A=110$  towards  $A=100$ .

The results in the vicinity of the doubly magic nucleus  $A=132$  show that the shell gap at  $N=82$  is larger than the experimental data suggests. Consequently, the shell effects with NL-SH are stronger than the empirical data. This is similar to what was also observed for the case of Ni isotopes at  $N=28$ . In comparison, NL3 shows shell effects which are slightly less stronger than those of NL-SH. However, the experimental difference in  $S_{2n}$  values of  $^{132}\text{Sn}$  and  $^{134}\text{Sn}$  is still overestimated by NL3.

The 2-neutron separation energies obtained with the scalar-vector self-coupling are shown in Fig. 15. The results with all the forces are in very good agreement with the experimental data over the whole mass range except for nuclei in the vicinity of the doubly magic  $A=132$ . Both NL-SV1 (a) and TM1 (c) overestimate slightly the experimental  $S_{2n}$  values for nuclei lighter than  $^{132}\text{Sn}$ . In comparison, the NL-SV2 results show an impressive agreement with the data almost over the whole mass range. For nuclei heavier than  $^{132}\text{Sn}$ , however, all the forces show a small divergence with the data.

Considering the shell gap at  $N=82$ , we observe that all the forces with the scalar-vector self-coupling in Fig. 15 are in good agreement with the experimental gap. This demonstrates that these forces reproduce the experimental shell gaps about  $N=82$  very well. Further, the presence of a well developed kink in  $S_{2n}$  values at  $A=132$  ( $N=82$ ) emphasizes that the shell effects in this region which is away from the stability line do remain strong. Indeed, this leads to a sharp reduction in the  $S_{2n}$  value of the isotope  $^{134}\text{Sn}$ . For nuclei heavier than this, the 2-neutron separation energies show only a mild decrease with the mass number. This is supported by the only experimental data point available at  $A=136$ . Theoretically, this behaviour is expected to be continued for heavier Sn isotopes as shown by another nucleus ( $A=138$ ) in Fig. 15. It may be mentioned that the neutron drip line in Sn nuclei is surmised to occur at very large mass number about  $A=170$ . It is expected that the 2-neutron separation energy would decrease very slowly to a vanishing value until the drip line is reached.

### 5.2.3 Single-Particle Levels

Figure 16 shows the neutron single-particle levels in the canonical basis for the nucleus  $^{102}\text{Sn}$  as obtained with the forces NL-SH and NL-SV2. It can be seen that with NL-SV2 the shell gap at  $N=50$  is reduced as compared to NL-SH. This reduction in the shell gap near the Fermi surface with the scalar-vector self-couplings was also observed for the Ni nuclei. A comparison of the single-particle levels obtained with the Skyrme force SkP shows that the level density with this force is generally higher than the RMF forces and that due to this reason the shell gaps are suppressed rather strongly. The shell gap at  $N=50$  is about half the shell gap in the RMF theory. This is illustrative of the quenching with the force SkP, which is much discussed in the literature [25, 40].

We show in Fig. 17 the single-particle levels for the nucleus  $^{134}\text{Sn}$ . We have chosen this nucleus in order to examine the shell gaps about the magic number  $N=82$ . The shell gap at  $N=82$  with NL-SV2 is smaller than with NL-SH and is consistent with the reduction in shell gap as reflected by the  $S_{2n}$  values about  $N=82$  in Fig. 15 as compared to NL-SH. In comparison, with the force SkP the shell gap at  $N=82$  is reduced significantly.

In order to review the situation on the shell effects at  $N=82$  with various mass models, we present in Fig. 18 the  $S_{2n}$  from FRDM, the ETF-SI and the mass model based upon infinite nuclear matter (INM) [48]. Although the mass formulae describe the  $S_{2n}$  values of most of the Sn isotopes correctly, there are differences in predictions about the shell closure. Comparison of  $S_{2n}$  values in the vicinity of  $A=132$  in Fig. 18a shows that the gap in the  $S_{2n}$  values about  $N=82$  is slightly smaller with FRDM than the experimental one implying that in the FRDM the  $N=82$  shell closure is slightly weaker. However, the shell effects with FRDM are still stronger as compared to the scenerio of the strong quenching with SkP in Fig. 9. The ETF-SI, on the other hand, is able to come closer to the experimental data. Thus, at  $N=82$  the ETF-SI demonstrates the shell effects which are stronger than FRDM. At  $N=50$  the shell effects with ETF-SI were also found to be strong and consistent with the experimental data. It may be reminded that at  $N=28$  the shell effects are strongly quenched in the ETF-SI as opposed to the experimental data.

In Fig. 18b we compare the predictions of the INM model [48] and SkP with the experimental data. The  $S_{2n}$  value from the INM model for  $^{134}\text{Sn}$  is much higher compared to the experimental one. The corresponding shell gap at  $N=82$  is consequently too small, implying a quenching of the shell effects. For all other isotopes, the  $S_{2n}$  values from the INM agree well with the experimental data. It may be mentioned that in the INM mass formula, determination of the nuclear matter properties and properties of finite nuclei is achieved on the basis of a model independent analysis of the available experimental data. However, the shell effects in the model seem to be quenched as seen at  $N=82$ .

The SkP results show agreement with the experimental data except for nuclei in the vicinity of the magic number. With SkP the shell gap at  $N=82$  is reduced as compared to the experimental data. The reduction in the shell gap at  $N=82$  (see Fig. 17) leads to an  $S_{2n}$  value for  $^{134}\text{Sn}$ , which is higher than the experimental one. This is indicative of a reduced shell strength with SkP at  $N=82$ . In contrast to the situation in Ni isotopes, it may, however, be stated that SkP does show a semblance of some shell strength at  $N=82$ . The quenching of the shell effects at  $N=82$  with SkP is not so strong as has been witnessed for the Ni isotopes at  $N=28$ . In comparison, a strong quenching was presented by SkP also at  $N=50$ . Therefore, contrary to the available experimental data, the quenching of the shell effects seems to be a generic feature of the force SkP.

## 6 Summary and Conclusions

We have studied the shell effects in nuclei about the stability line in the RMF theory. The chains of Ni and Sn isotopes have been considered, where experimental data over a large range of isospin are available. First, employing the existing forces NL-SH and NL3 with the non-linear scalar self-coupling of  $\sigma$ -meson, we have investigated the ground-state properties of the Ni and Sn isotopic chains. It is shown that in the RMF+BCS approach where the pairing gaps are taken from the experimental data, the experimental binding energies of Ni isotopes are described well. Calculations within the RHB approach with the self-consistent finite-range pairing show only a slight improvement over the RMF+BCS

results in this isotopic chain. This shows that the RMF+BCS approach in conjunction with the pairing gaps obtained from the experimental data suffices to bring about a good description of the binding energies of the Ni isotopes. However, the same can not be said for the Sn isotopes. The pairing correlations for Sn nuclei are not adequately described within the BCS scheme. It is shown that for these nuclei, the RHB approach with the self-consistent pairing is necessary in order to get a good agreement with the binding energies.

In addition to the nonlinear scalar coupling of  $\sigma$  meson, we have introduced nonlinear vector self-coupling of  $\omega$  meson in the RHB approach. The self-consistent pairing is included by taking the finite-range Gogny force in the p-p channel. We have employed the recently developed forces NL-SV1 and NL-SV2 and the force TM1. It is shown that the RHB approach with the non-linear scalar-vector self-couplings provides a very good description of the binding energies of Ni and Sn isotopes.

We have investigated the shell effects in nuclei about the stability line within the two model Lagrangians, i.e. the RHB theory with the non-linear scalar self-coupling of  $\sigma$ -meson only and the RHB theory with the non-linear self-couplings of both  $\sigma$  and  $\omega$  mesons. The experimental data on 2-neutron separation energies of Ni and Sn isotopes have been used. The sharp decrease in the  $S_{2n}$  values about a magic number is taken as a measure of the shell gap. The experimental data on Ni encompass the magic number N=28, whilst the magic number N=82 is encompassed by the Sn data. It is shown that the forces with the non-linear scalar self-coupling give shell gaps which are larger than suggested by the experimental data. This is found to be the case for N=28 in Ni isotopes as well as for N=82 in Sn isotopes.

The results with the Lagrangian with the scalar-vector self-couplings show that the force NL-SV2 describes the experimental data on the 2-neutron separation energies very well. The shell effects about the magic numbers in Ni and Sn isotopes with the scalar-vector self-couplings are shown to be consistent with the experimental data. The single-particle spectra for the Ni and Sn nuclei in the vicinity of magic numbers show that the

shell gaps at  $N=28$ ,  $N=50$  and  $N=82$  are smaller in the model with the scalar-vector self-couplings as compared to the scalar self-coupling only.

A comparison of the experimental data and the results of the scalar-vector self-coupling model with the HFB results using the Skyrme force SkP for the Ni isotopes has shown that the shell effects with SkP are quenched strongly at  $N=28$ . This is contrary to the experimental data which show that the shell effects are substantially stronger. The weak or quenched shell effects are also shown in Ni isotopes by SkP at  $N=50$ . The quenching of the shell effects with the force SkP is demonstrated by the corresponding single-particle spectra for  $^{58}\text{Ni}$ ,  $^{80}\text{Ni}$  and  $^{134}\text{Sn}$ , whereby the shell gaps at  $N=28$ ,  $N=50$  and  $N=82$ , respectively are considerably smaller than the RHB single-particle gaps. In summary, the quenching of the shell effects seems to be an artifact of the force SkP and is not supported by the experimental data. The substantial reduction in the shell gaps with SkP stems from the correspondingly high level density. This is due to a large effective mass being chosen for this force.

It is expected that due to inherently different single-particle structure in each model the shell effects at the stability line would have varying consequences on the shell effects at the drip lines. It was shown earlier [26] that with the non-linear scalar self-coupling in the RMF theory shell effects near the neutron drip line in the vicinity of  $N=82$  were predicted to be strong. This conclusion was based upon RMF theory with the BCS pairing using the force NL-SH. It was also shown [26] that the pairing itself does not create or destroy the shell effects. The conclusions of the strong shell effects near the neutron drip line were contested [27]. It was suggested on the basis of HFB calculations with SkP that the shell effects near the drip line quench strongly. In the light of the forgoing discussions, it is only expected that the shell gap at  $N=82$  with the force SkP would diminish. Thus, the quenching of the shell effects near the drip line at  $N=82$  with the force SkP is in complete accord with the quenching shown by it near the stability line. This quenching is, however, not supported by the experimental data at the stability line as demonstrated in this work.

As shown above, the force NL-SH with the scalar coupling gives shell effects which are slightly stronger than the experimental data. This fact notwithstanding, we have performed a study [44] to investigate the role of the vector self-coupling on shell effects at the drip line. It is observed that with the scalar-vector self-couplings which describes the shell effects at the stability line well, shell effects near the neutron drip line are slightly less stronger than with the scalar self-coupling only. However, we do not find indications of any shell quenching. Details of this work will be provided elsewhere [44].

It may be noted that in the fits of the r-process abundances [40], HFB results based upon the force SKP were used. It was shown [40] that the HFB results give an improved fit to the global r-process abundances. Since the force SkP is known to quench shell effects as shown above, it was concluded on this basis that the shell effects at  $N=82$  at the neutron drip line are quenched. However, as discussed in our work, this quenching with SkP is not consistent with the experimental data. Thus, an improved fit to r-process abundances using the SkP results may be insufficient to assert the shell quenching at  $N=82$  near the neutron drip-line, notwithstanding an overwhelming shell quenching with SkP.

## 7 Acknowledgment

This research was supported by the Kuwait University Research Administration through the Project No. SP056. We thank Prof. J. Dobaczewski for supplying the HFB results on Ni isotopes.

## References

- [1] B.D. Serot and J.D. Walecka, *Adv. Nucl. Phys.* **16** (1986) 1.
- [2] P.G. Reinhard, *Rep. Prog. Phys.* **52** (1989) 439.
- [3] Y.K. Gambhir, P. Ring, and A. Thimet, *Ann. Phys. (N.Y.)* **198** (1990) 132.
- [4] B.D. Serot, *Rep. Prog. Phys.* **55** (1992) 1855.
- [5] M.M. Sharma, M.A. Nagarajan, and P. Ring, *Phys. Lett.* **B312** (1993) 377.
- [6] P. Ring, *Prog. Part. Nucl. Phys.* **37** (1996) 193.
- [7] B.D. Serot and J.D. Walecka, *Mod. Phys.* **E6** (1997) 515.
- [8] M.M. Sharma, G.A. Lalazissis, and P. Ring, *Phys. Lett.* **B317** (1993) 9.
- [9] E.W. Otten, in *Treatise on Heavy-Ion Science*, Vol. 7, ed. D.A. Bromley (Plenum, New York, 1989).
- [10] N. Tajima, P. Bonche, H. Flocard, P.-H. Heenen and M.S. Weiss, *Nucl. Phys.* **A551** (1993) 434.
- [11] M.M. Sharma, G.A. Lalazissis, J. König, and P. Ring, *Phys. Rev. Lett.* **74** 3744 (1994).
- [12] D. Von-Eiff, H. Freyer, W. Stocker and M.K. Weigel, *Phys. Lett.* **B344** (1995) 11.
- [13] G.A. Lalazissis, A.R. Farhan and M.M. Sharma, *Nucl. Phys.* **A628** (1998) 221.
- [14] T. Gonzales-Llarena, J. Egidio, G.A. Lalazissis and P. Ring, *Phys. Lett.* **B379** (1996) 13.
- [15] G.A. Lalazissis, D. Vretenar and P. Ring, *Phys. Rev.* **C57** (1998) 2294.
- [16] J. Meng, *Nucl. Phys.* **A635** (1998) 3.
- [17] M.G. Mayer and J.H.D. Jensen, *Elementary Theory of Nuclear Shell Structure* (Wiley, New York, 1955).
- [18] D. Vautherin and D.M. Brink, *Phys. Rev.* **C7** (1973) 296.
- [19] C. Borcea, G. Audi, A.H. Wapstra and P. Favaron, *Nucl. Phys.* **A565** 158 (1993).
- [20] E. Roeckel, *Rep. Prog. Phys.* **55** (1992) 1661.
- [21] A. Mueller and B. Sherril, *Ann. Rev. Nucl. Part. Sci.* **43** (1993) 529.
- [22] I. Tanihata, *Progr. Part. Nucl. Phys.* **35** (1996) 435. (1995) 505.
- [23] J. Vervier, *Prog. Part. Nucl. Phys.* **37** (1996) 435.
- [24] Proc. 4th Int. Conf. on Radioactive Nuclear Beams, Omiya, Japan, *Nucl. Phys.* **A616** (1997).
- [25] K.-L. Kratz, J.P. Bitouzet, F.K. Thielemann, P. Möller and B. Pfeiffer, *Astrophys. J.* **403** (1993) 216.

- [26] M.M. Sharma, G.A. Lalazissis, W. Hillebrandt, and P. Ring, Phys. Rev. Lett. **72** (1994) 1431; *ibid* **73** (1994) 1870.
- [27] J. Dobaczewski, I. Hamamoto, W. Nazarewicz and J.A. Sheikh, Phys. Rev. Lett. **72** (1994) 981.
- [28] A.R. Bodmer, Nucl. Phys. **A526** (1991) 703.
- [29] Y. Sugahara and H. Toki, Nucl. Phys. **A579** (1994) 557.
- [30] H. Müller and B.D. Serot, Nucl. Phys. **A606** (1996) 508.
- [31] M.M. Sharma (1999, in preparation)
- [32] J. Boguta and A.R. Bodmer, Nucl. Phys. **A292** (1977) 413.
- [33] R.J. Furnstahl, B.D. Serot and H.B. Tang, Nucl. Phys. **A598** (1996) 539.
- [34] J. Dobaczewski, H. Flocard and J. Treiner, Nucl. Phys. **A422** (1984) 103.
- [35] H. Kucharek and P. Ring, Z. Phys. **A339** (1991) 23.
- [36] J.F. Berger, M. Girod and D. Gogny, Nucl. Phys. **A428** (1984) 32.
- [37] G.A. Lalazissis, J. König and P. Ring, Phys. Rev. **C55** (1997) 540.
- [38] G.A. Lalazissis, D. Vretenar, W. Pöschl and P. Ring, Nucl. Phys. **A632** (1998) 363.
- [39] G. Audi and A.H. Wapstra, Nucl. Phys. **A595** (1995) 409.
- [40] B. Chen, J. Dobaczewski, K.-L. Kratz, K. Langanke, B. Pfeiffer, F.-K. Thielemann and P. Vogel, Phys. Lett. **B355** (1995) 37.
- [41] J.M. Pearson, R.C. Nayak and S. Goriely, Phys. Lett. **B387** (1996) 455.
- [42] K.L. Kratz, B. Pfeiffer and F.-K. Thielemann, Nucl. Phys. **A630** (1998) 352c.
- [43] J. Dobaczewski, private communication (1994).
- [44] A.R. Farhan and M.M. Sharma, in preparation (1999).
- [45] M.M. Sharma, RIKEN Review No. 23 (1999) 106 and preprint nucl-th/9904036, Los Alamos National Laboratory (1999).
- [46] P. Möller, J.R. Nix, W.D. Myers and W.J. Swiatecki, At. Data Nucl. Data Tables **59** (1995) 185.
- [47] Y. Aboussir, J.M. Pearson, A.K. Dutta and F. Tondeur, At. Data Nucl. Data Tables **61** (1995) 127.
- [48] L. Satpathy, V.S. Uma Maheshwari and R.C. Nayak, Phys. Rep. **319** (1999) 85.

## Figure Captions

- Fig. 1** Binding energy of Ni isotopes with respect to the experimental values, in (a) RMF approach with BCS pairing and (b) RHB approach with self-consistent finite-range pairing, using the forces NL-SH and NL3 with the non-linear scalar self-coupling of  $\sigma$  meson.
- Fig. 2** The same as in Fig. 1, with the forces NL-SV1, NL-SV2 and TM1 with the non-linear scalar-vector self-coupling.
- Fig. 3** The 2-neutron separation energy  $S_{2n}$  of Ni isotopes using the forces with the non-linear scalar self-coupling (a) NL-SH and (b) NL3. A comparison of the RMF+BCS and RHB values is made with the experimental data.
- Fig. 4** The  $S_{2n}$  values for Ni isotopes in (a) RMF+BCS and (b) RHB approach. Within each approach, a comparison of the results of the forces NL-SH and NL3 is made with the experimental data.
- Fig. 5** The  $S_{2n}$  values for Ni isotopes in (a) RMF+BCS and (b) RHB approach with the forces with the non-linear scalar and vector self-coupling. A comparison of the results of the forces NL-SV2 and TM1 is made with the experimental data.
- Fig. 6** A comparison of the 2-neutron separation energy  $S_{2n}$  of Ni isotopes using the force NL-SH with the scalar self-coupling and using the force NL-SV2 with the scalar-vector self-coupling in RHB. The results are shown in the region of closed neutron shell (a) N=28 (A=56) and (b) N=50 (A=78). A comparison with the experimental data is made. The results from the HFB approach with the Skyrme force SkP are also shown for comparison [43].
- Fig. 7** The neutron single-particle spectrum for the nucleus  $^{58}\text{Ni}$  calculated in the canonical basis in RHB with the forces NL-SH and NL-SV2. A reduction in the shell gap at N=28 with the force NL-SV2 can be seen, as compared to NL-SH. The corresponding spectrum for SkP shows a drastic reduction in the N=28 shell gap.
- Fig. 8** The same as Fig. 7, for the nucleus  $^{80}\text{Ni}$ . The shell gap at N=50 with the force SkP is significantly reduced as compared to that with NL-SH and NL-SV2.
- Fig. 9** The  $S_{2n}$  values in the region (a) N=28 and (b) N=50 from the mass models FRDM, ETF-SI and the HFB approach with SkP. A comparison is made with the experimental data available.
- Fig. 10** The binding energies of Sn isotopes in the (a) RMF+BCS and (b) RHB approach with the forces NL-SH and NL3.
- Fig. 11** A comparison of the binding energies of Sn nuclei in the RMF+BCS and RHB approach with the forces (a) NL-SH and (b) NL3. A smoothening of the energies in the RHB is observed.
- Fig. 12** The binding energies of Sn nuclei using the forces with the vector self-coupling of  $\omega$  meson (a) NL-SV1, (b) NL-SV2 and (c) TM1, compared with the experimental values, in RMF+BCS and RHB approach.
- Fig. 13** The binding energies of Sn isotopes obtained with the RHB approach with the self-consistent pairing. A comparison is made between the results from the forces NL-SV1, NL-SV2 and TM1.

**Fig. 14** The  $S_{2n}$  values for Sn isotopes obtained in the RHB approach with the forces (a) NL-SH and (b) NL3. The experimental data about A=132 shows a strong kink indicating strong shell effects about N=82.

**Fig. 15** The  $S_{2n}$  values for Sn isotopes obtained in the RHB approach with the forces (a) NL-SV1, (b) NL-SV2 and (c) TM1. The experimental data are shown for the comparison.

**Fig. 16** The neutron single-particle spectrum of  $^{102}\text{Sn}$  obtained in the canonical basis in the RHB approach with the forces NL-SH and NL-SV2. The levels with the force SkP are also shown for comparison.

**Fig. 17** The same as Fig. 16, for  $^{134}\text{Sn}$ .

**Fig. 18** A comparative view of the  $S_{2n}$  values for Sn isotopes from the mass models FRDM [46], ETF-SI [47], and INM model [48] in the region about N=82.

Table 1: The Lagrangian parameters of the forces with the non-linear scalar self-coupling NL-SH, NL3, and the forces with the scalar-vector self-coupling NL-SV1, NL-SV2 and TM1 used in the calculations.

	NL-SH	NL3	NL-SV1	NL-SV2	TM1
M	939.0	939.0	939.0	939.0	938.0
$m_\sigma$	526.05921	508.1941	510.03488	519.81202	511.198
$m_\omega$	783.0	782.5010	783.	783.0	783.0
$m_\rho$	763.0	763.0	763.	763.0	770.0
$g_\sigma$	10.44355	10.2169	10.12479	10.32001	10.0289
$g_\omega$	12.9451	12.8675	12.72661	12.88233	12.6139
$g_\rho$	4.38281	4.4744	4.49197	4.50144	4.6322
$g_2$	-6.90992	-10.4307	-9.24058	-6.86061	-7.2325
$g_3$	-15.83373	-28.8851	-15.388	0.36754	0.6183
$g_4$	0.0	0.0	41.01023	72.38965	71.30750

Fig. 1

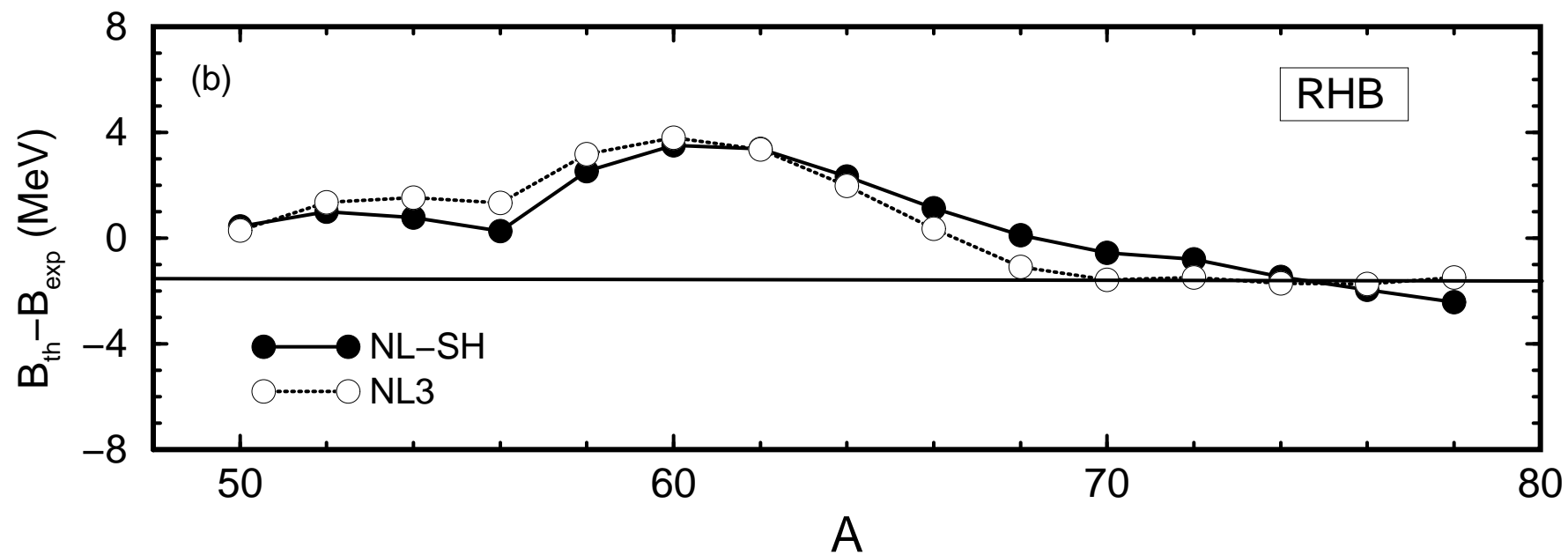
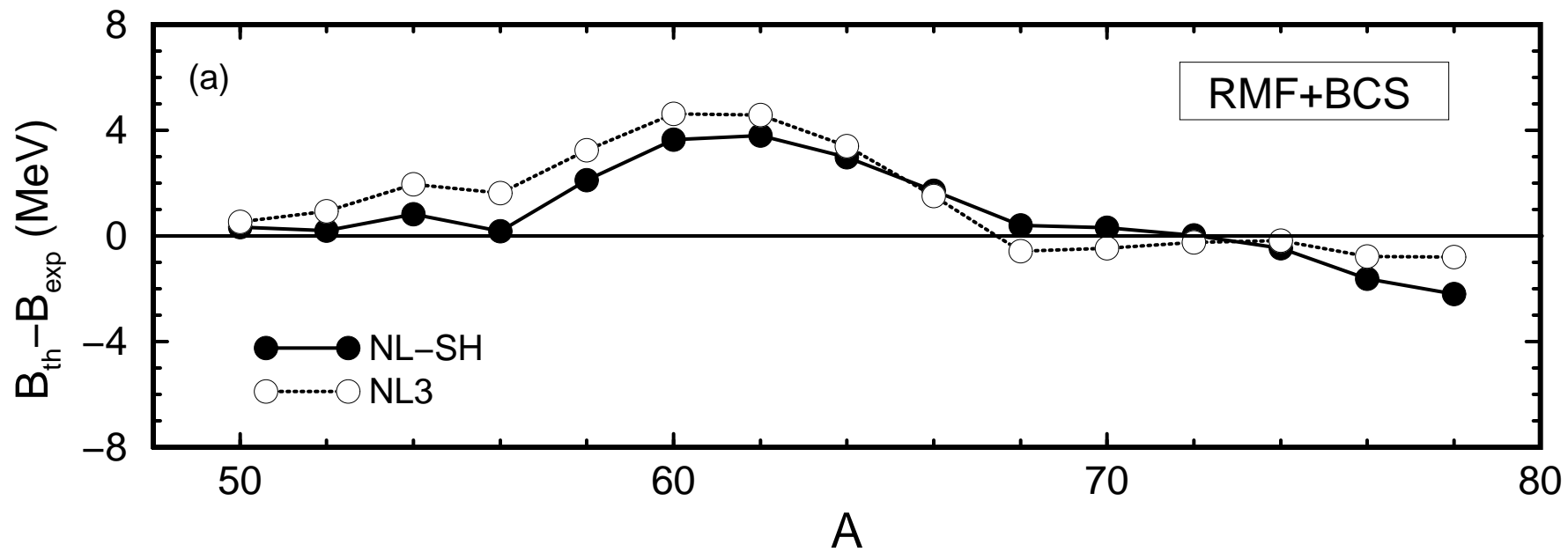
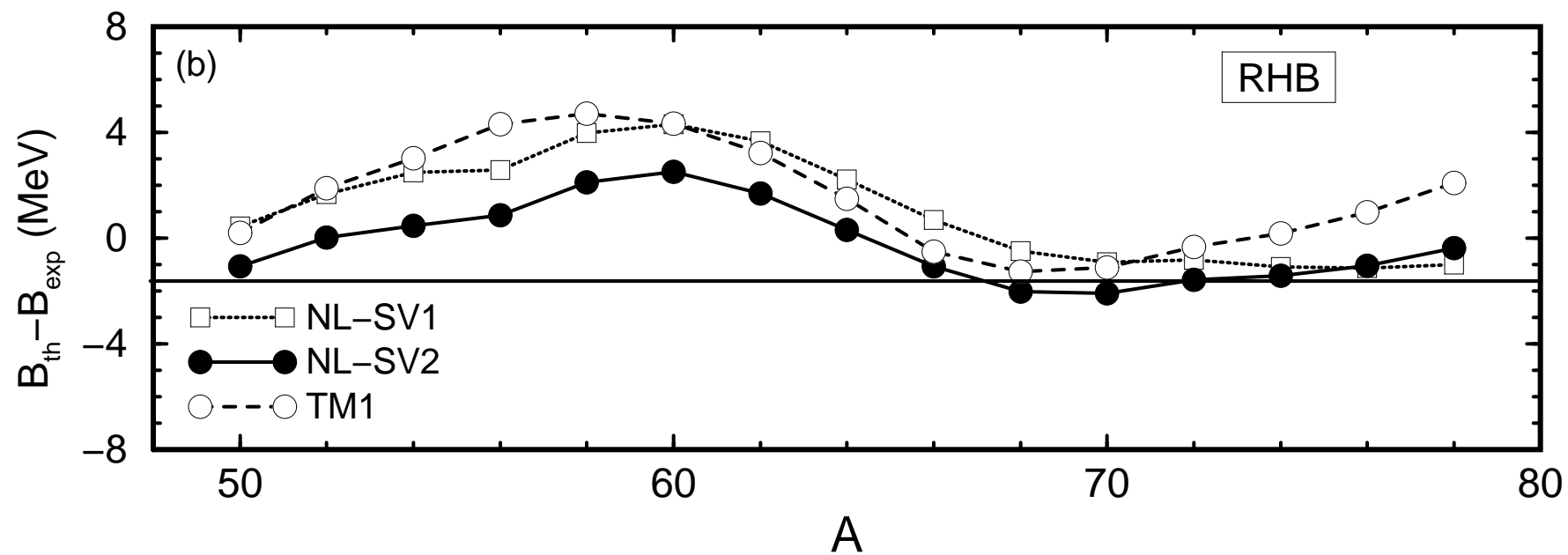
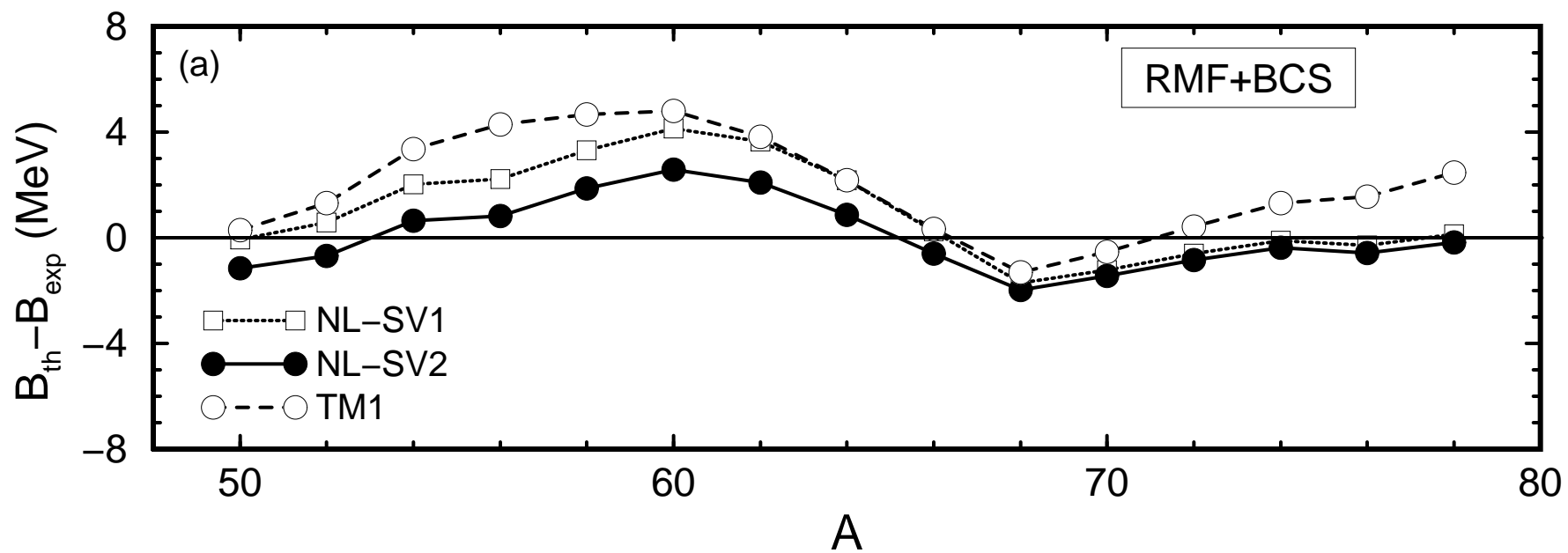


Fig. 2



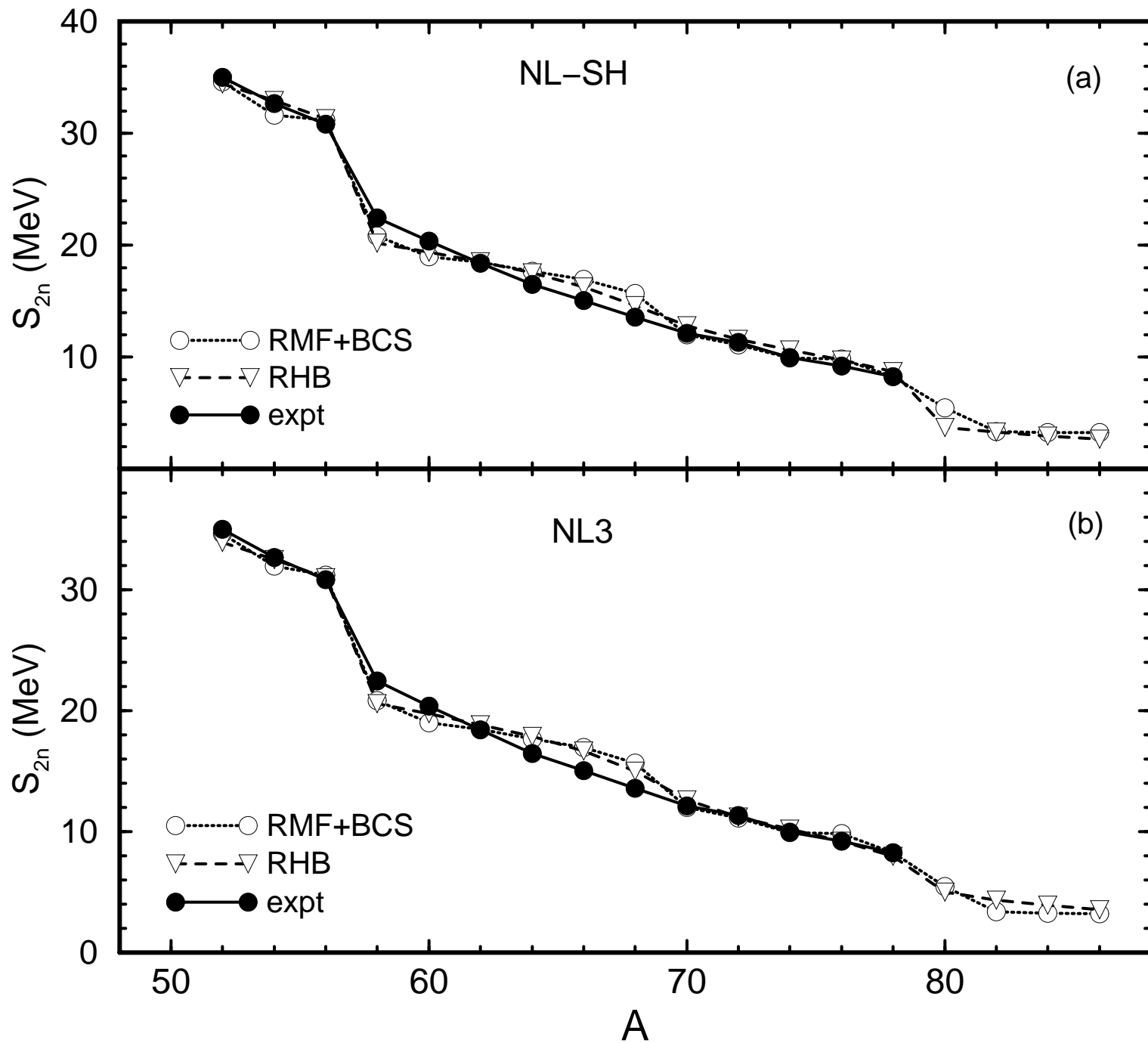


Fig. 3

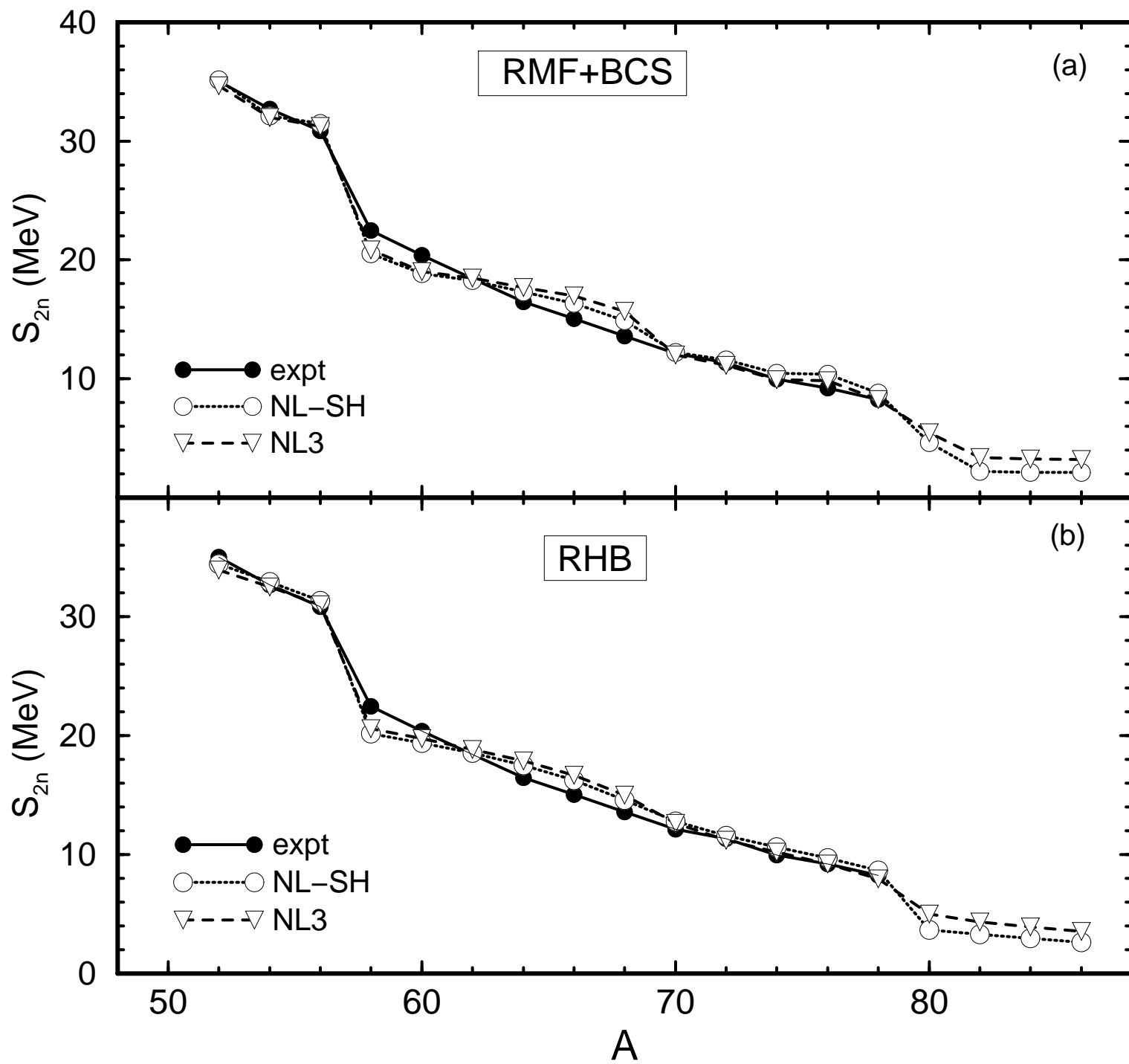


Fig. 4

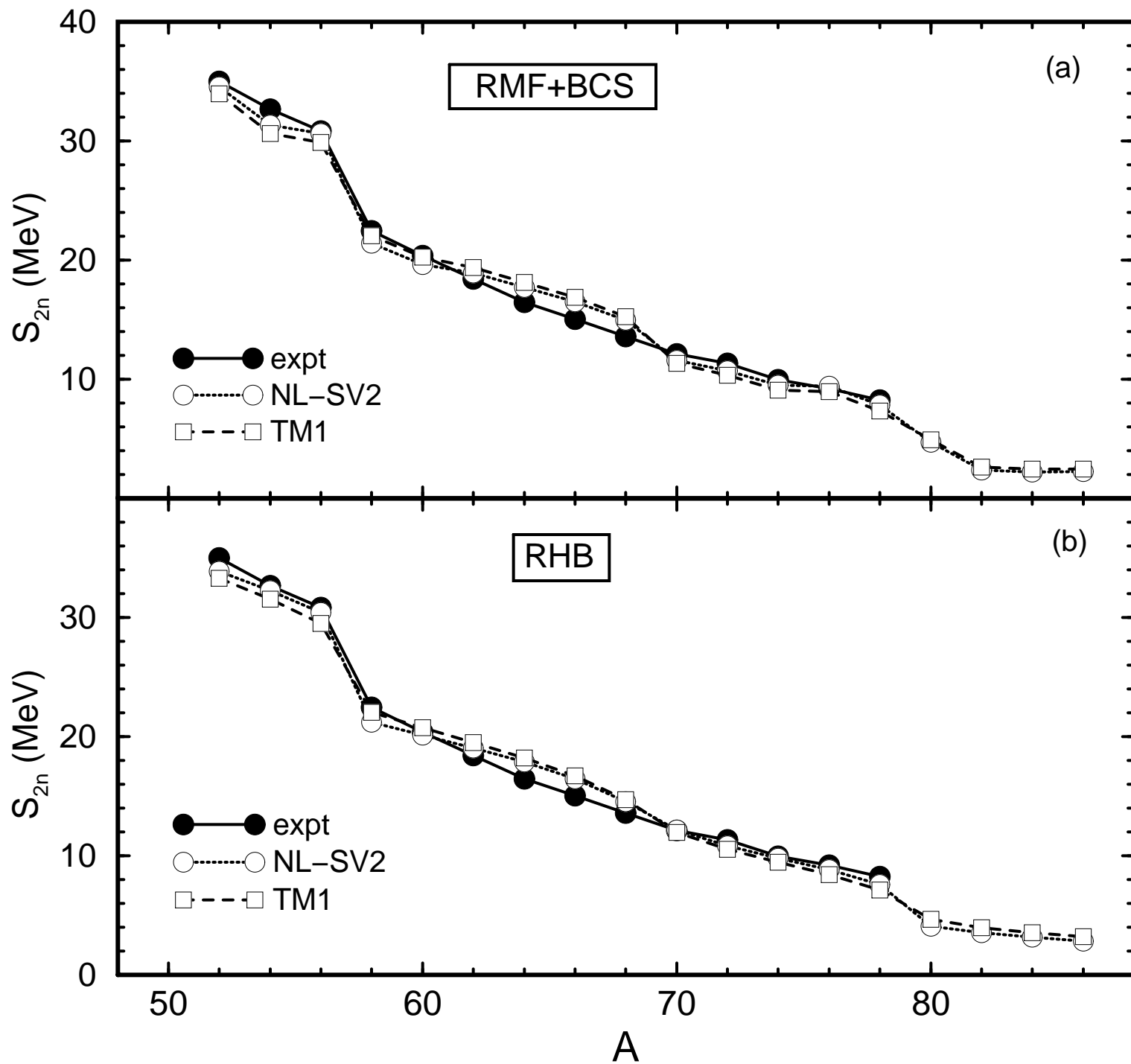
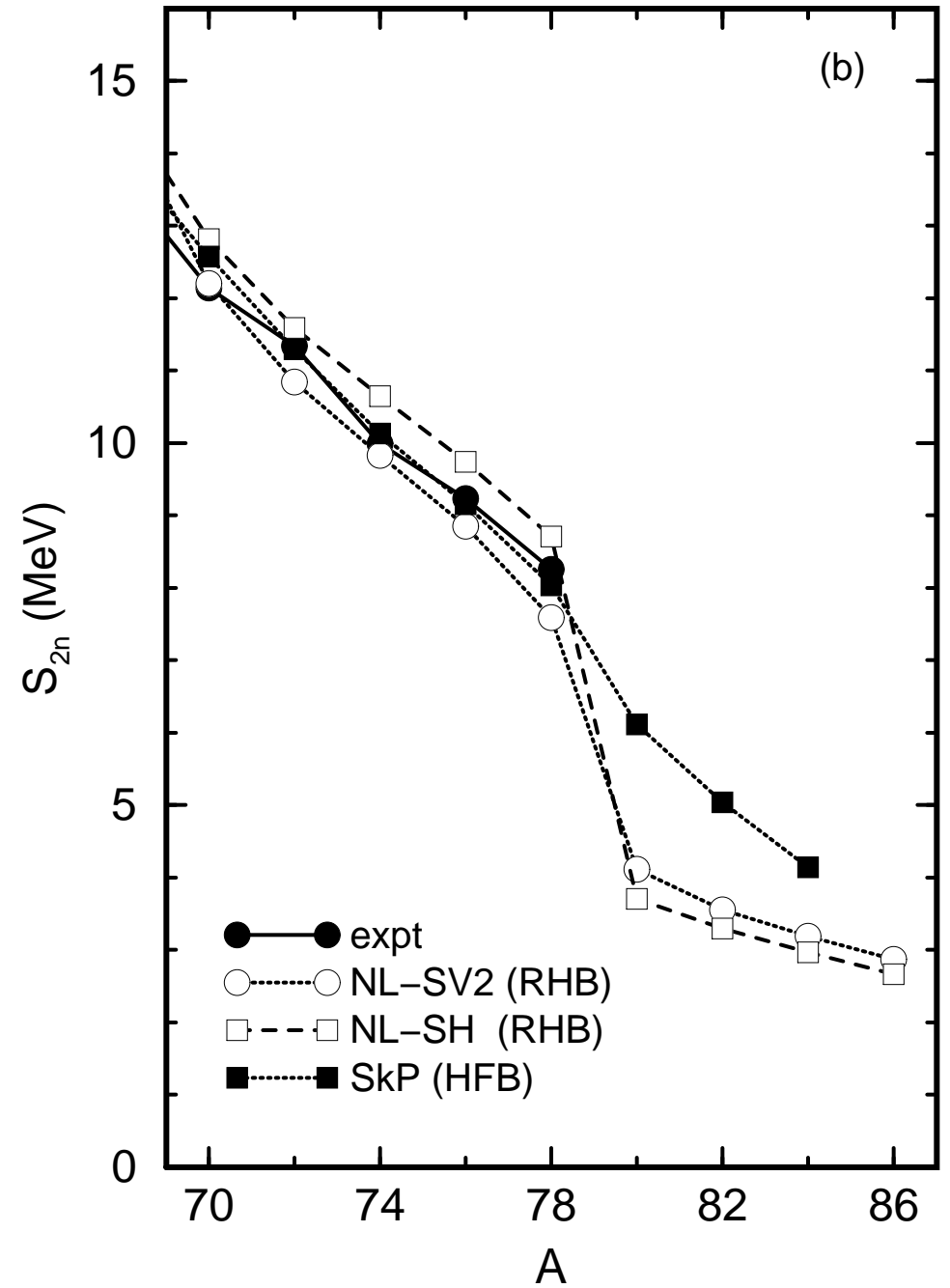
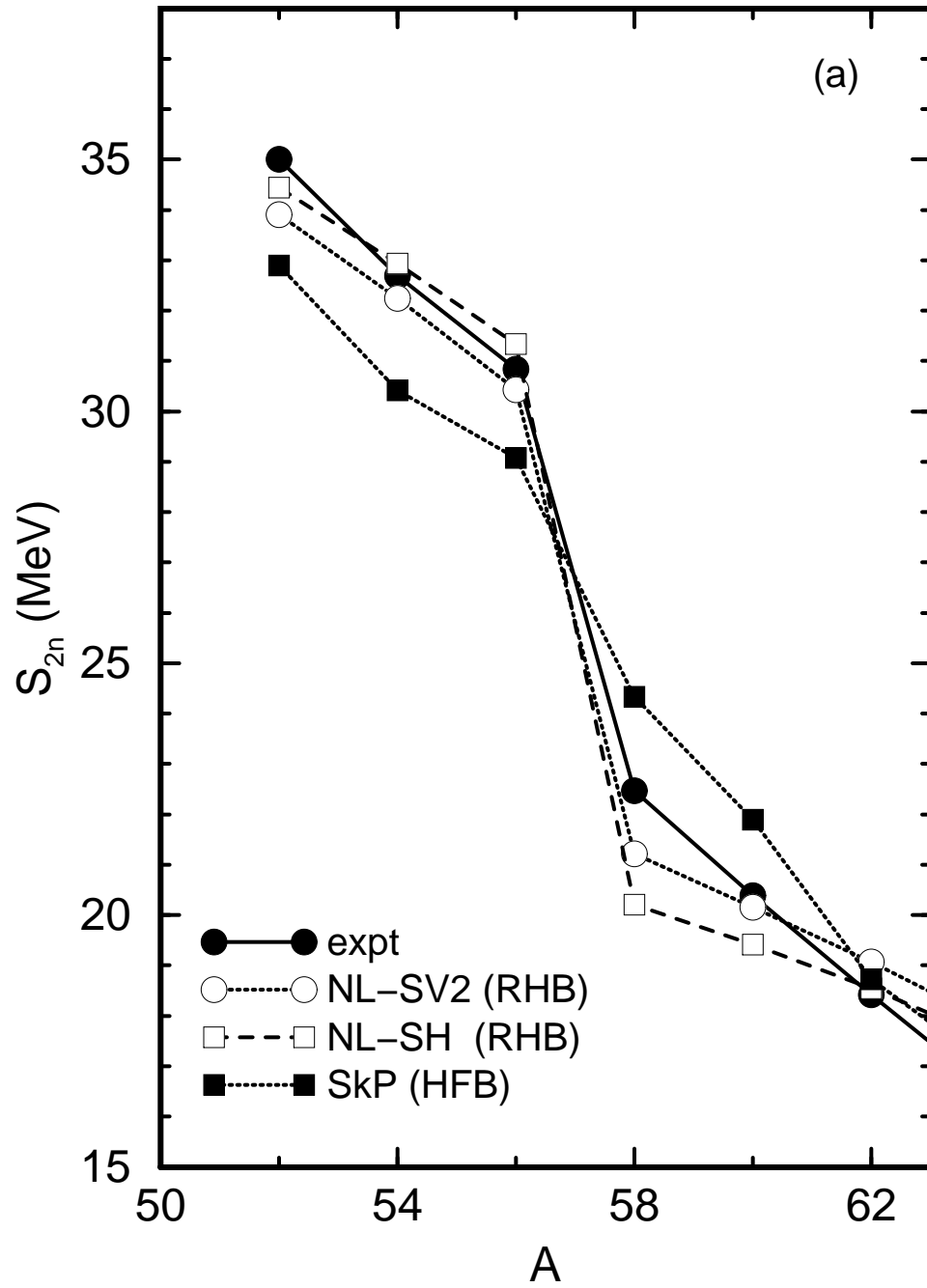


Fig. 5

Fig.6



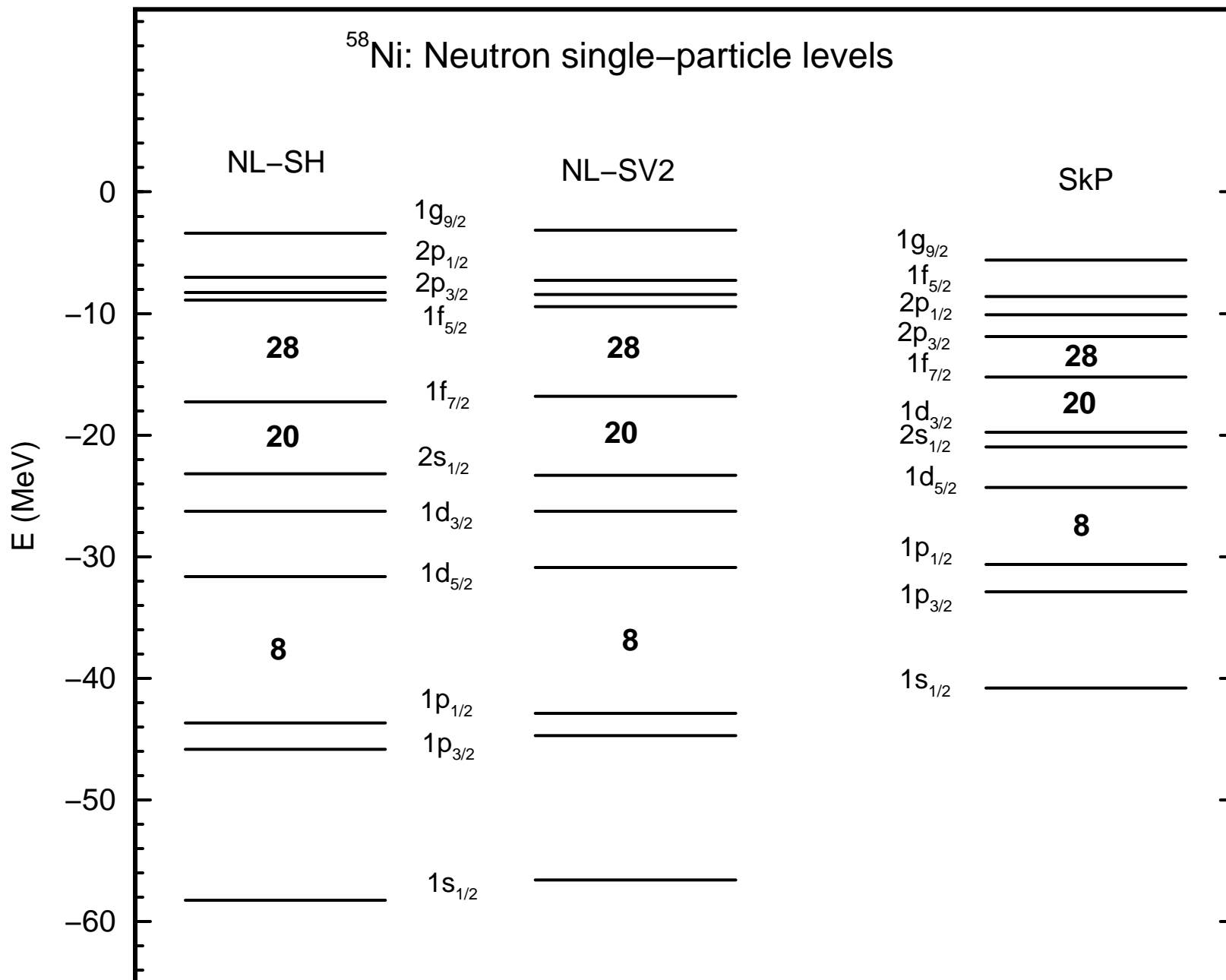


Fig. 7

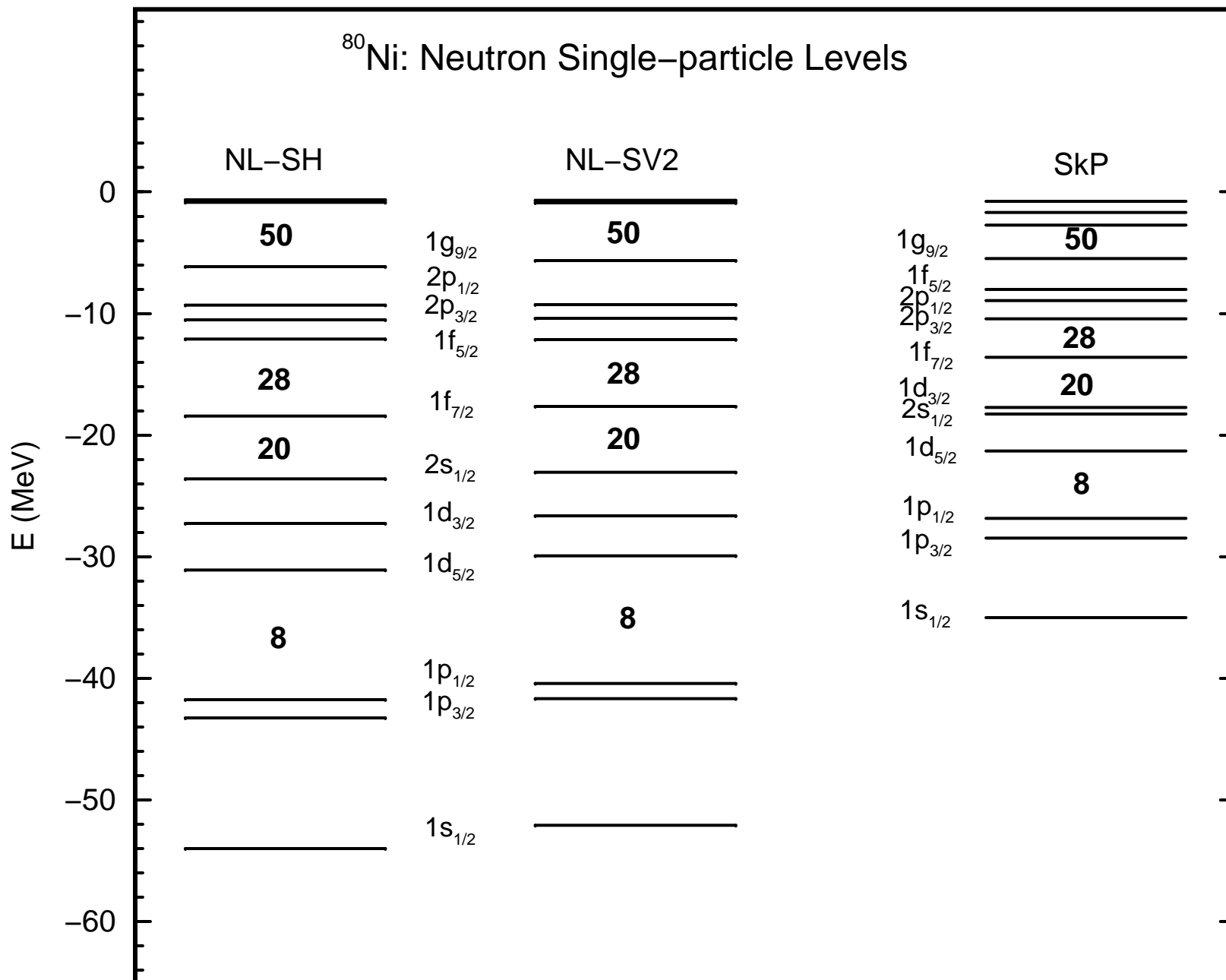
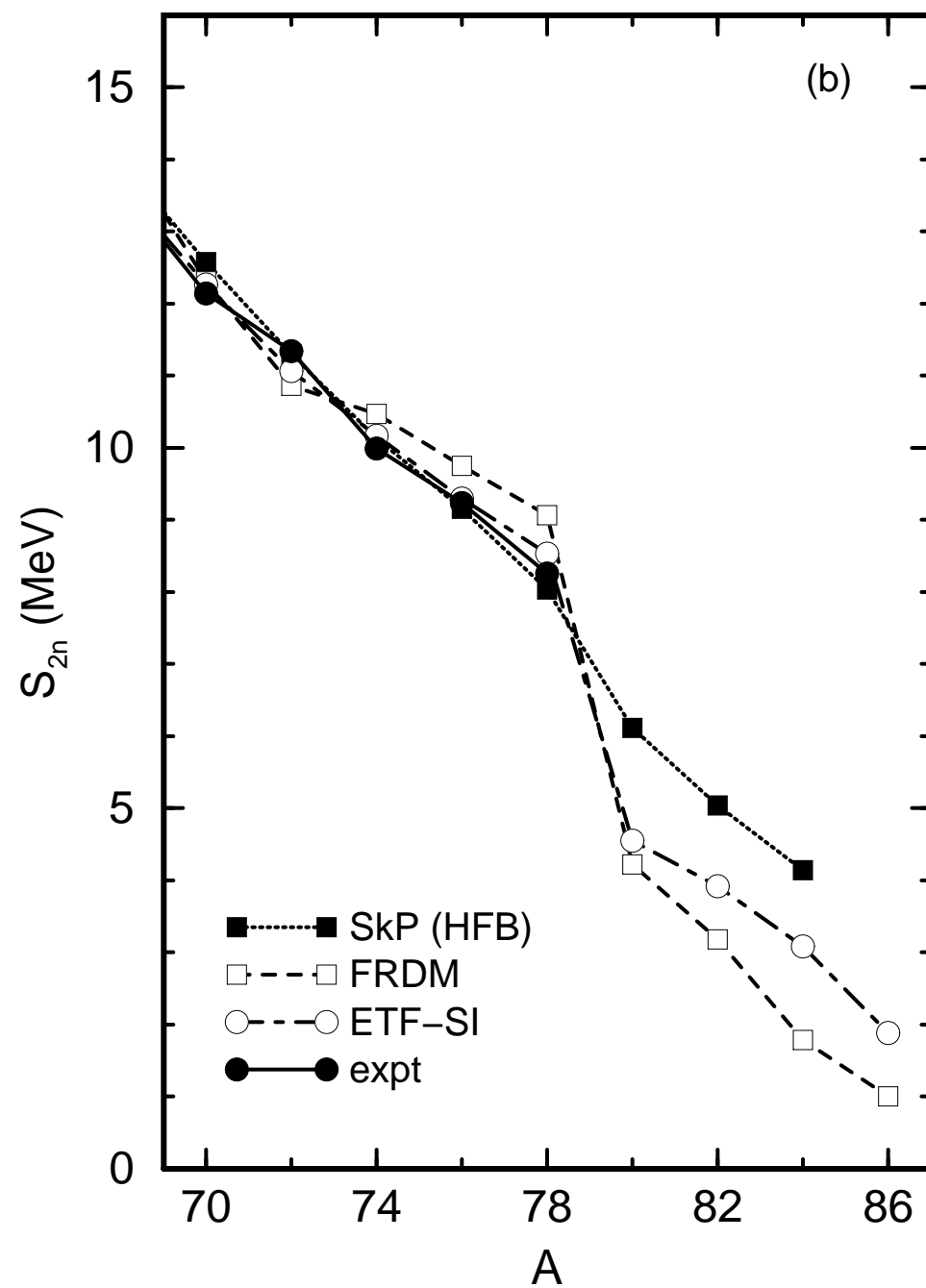
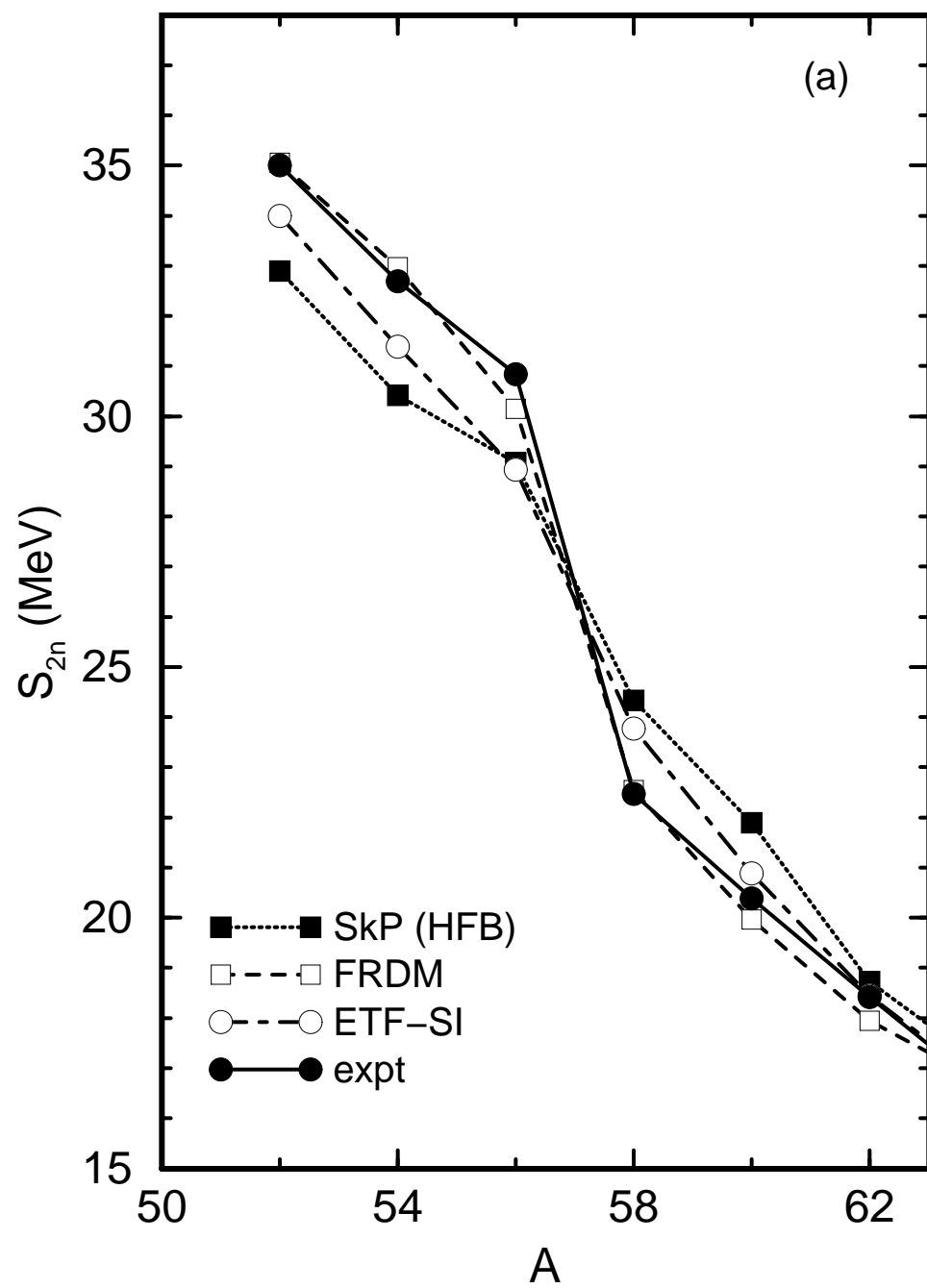


Fig. 8

Fig. 9



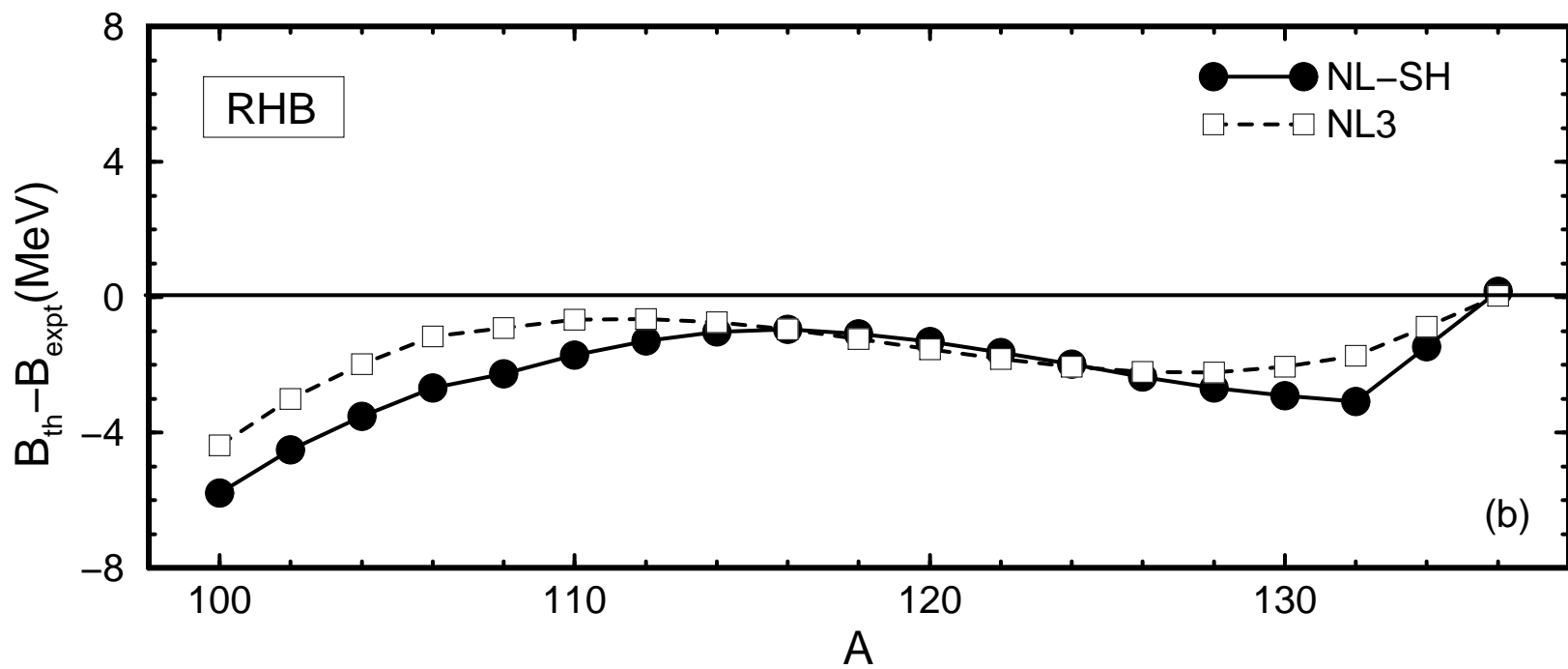
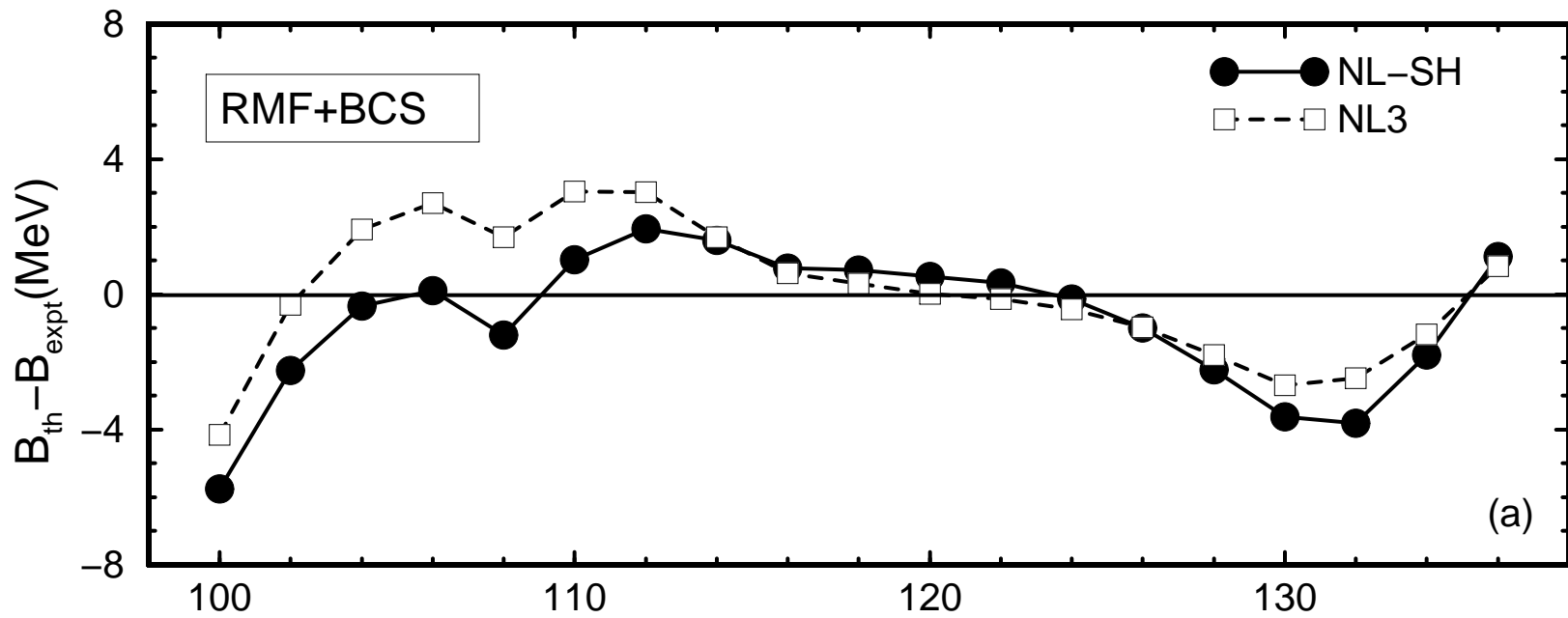


Fig. 10

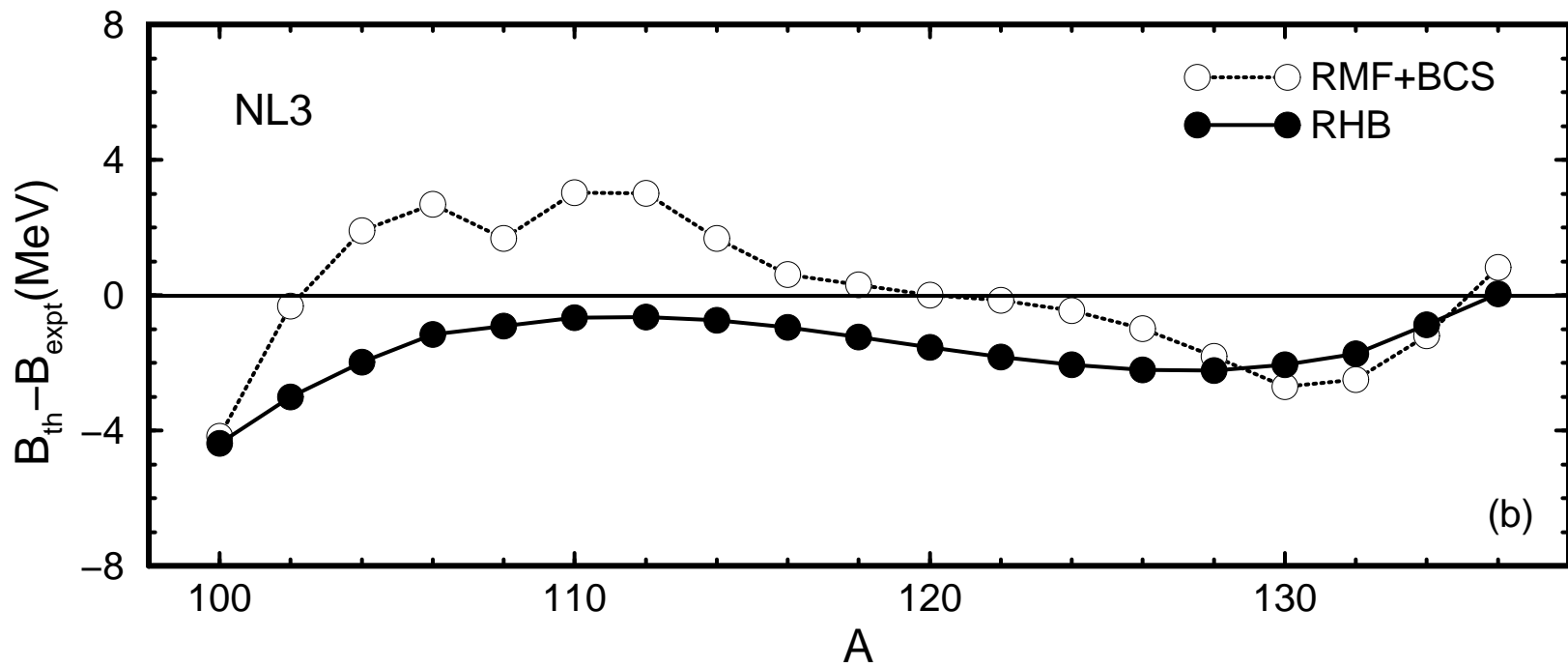
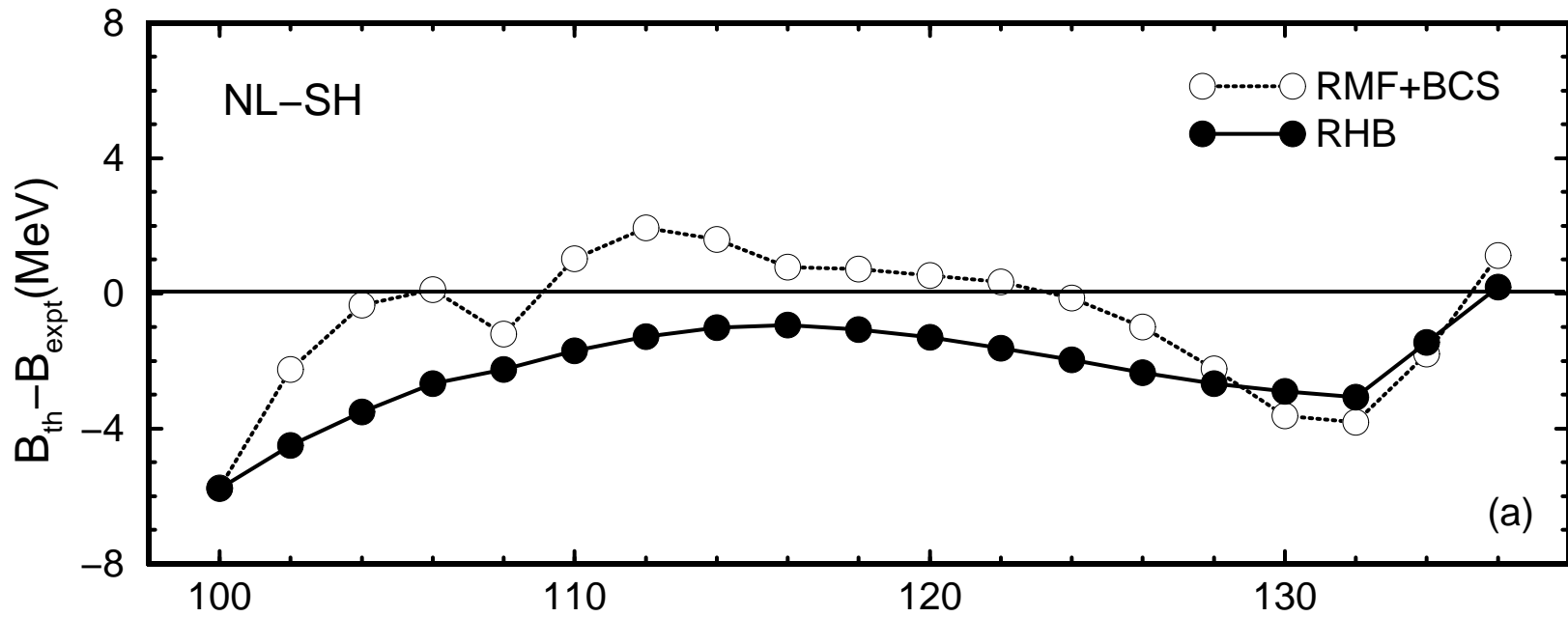


Fig. 11

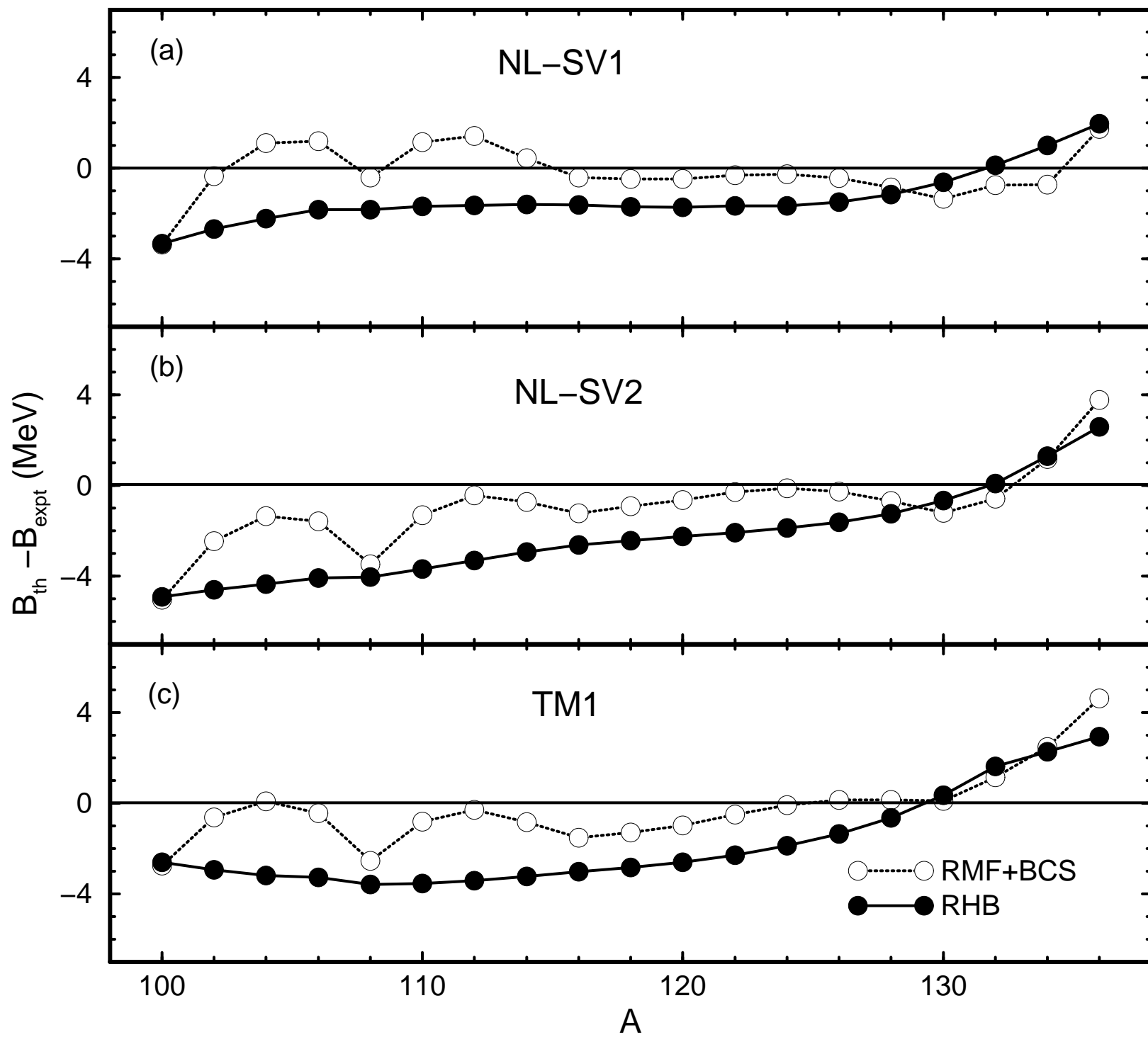


Fig. 12

Fig. 13

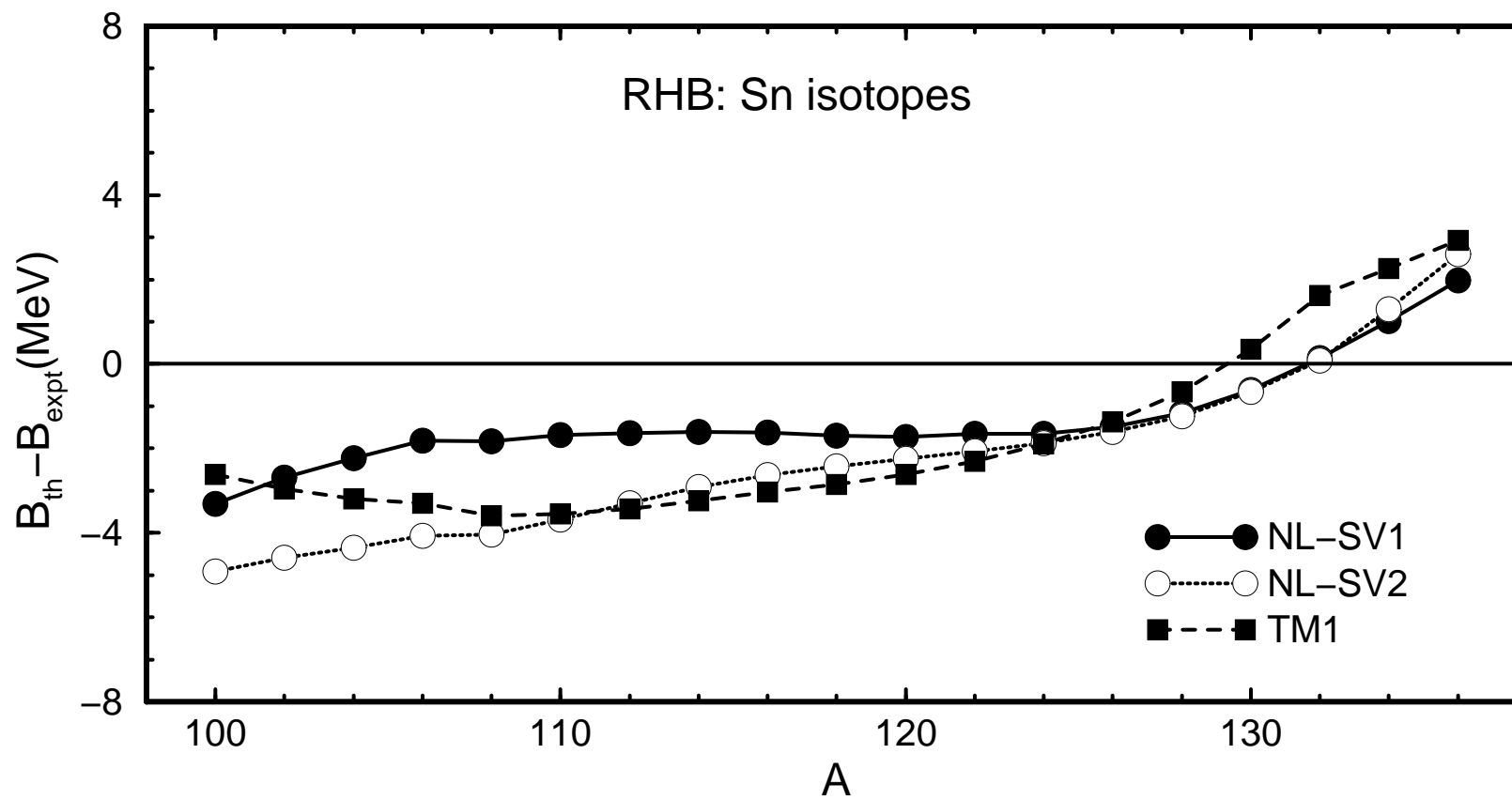
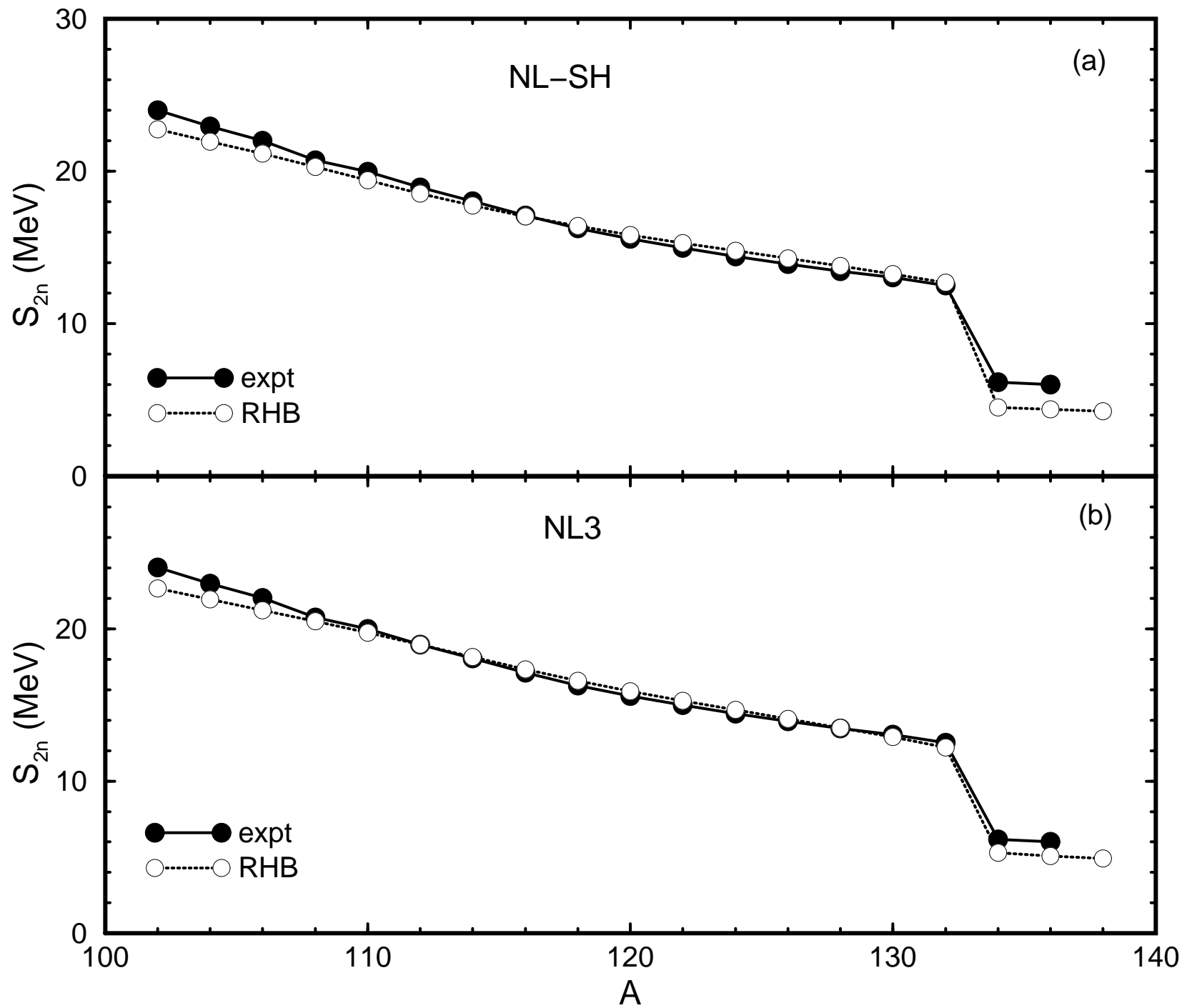


Fig. 14



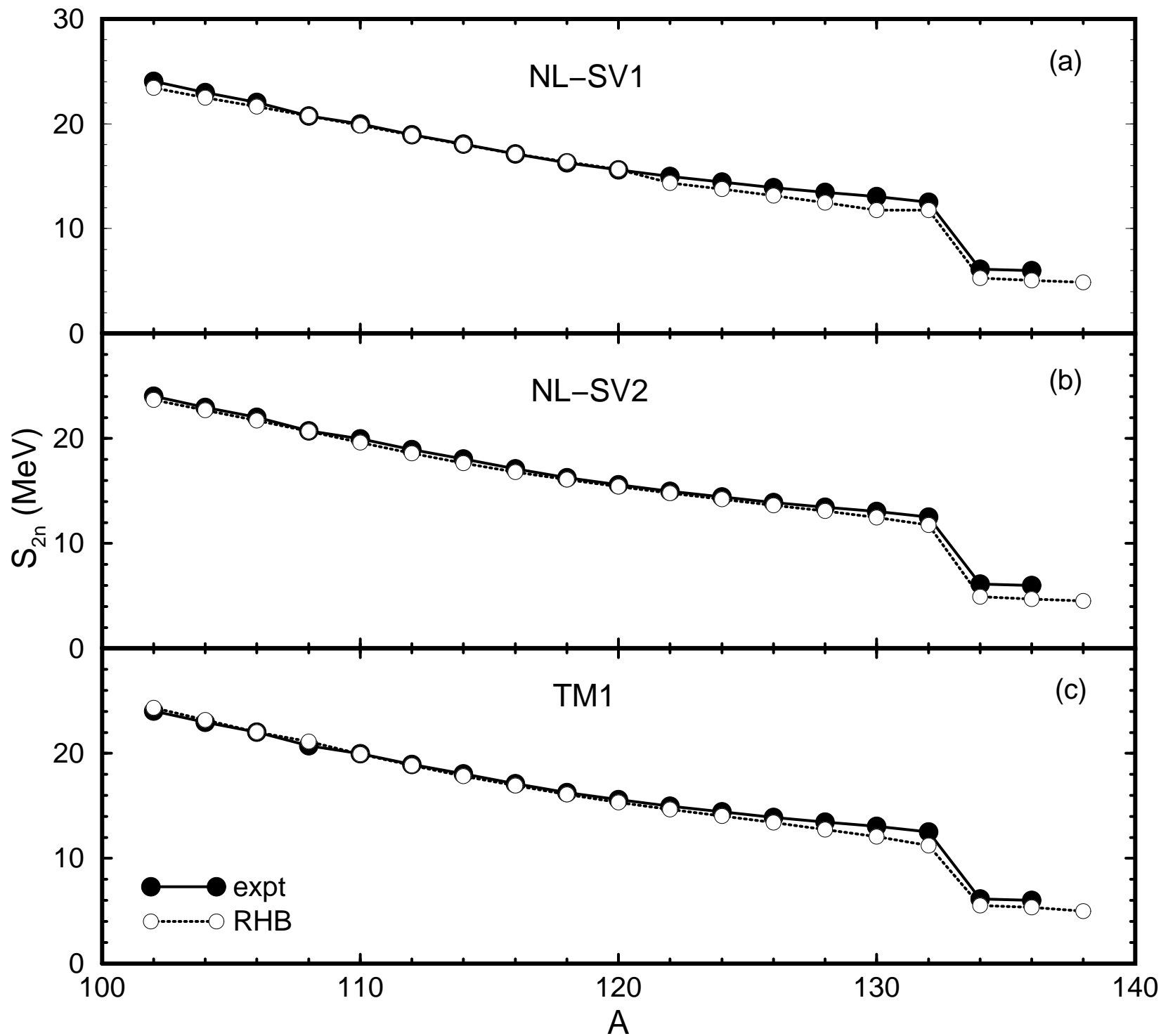


Fig. 15

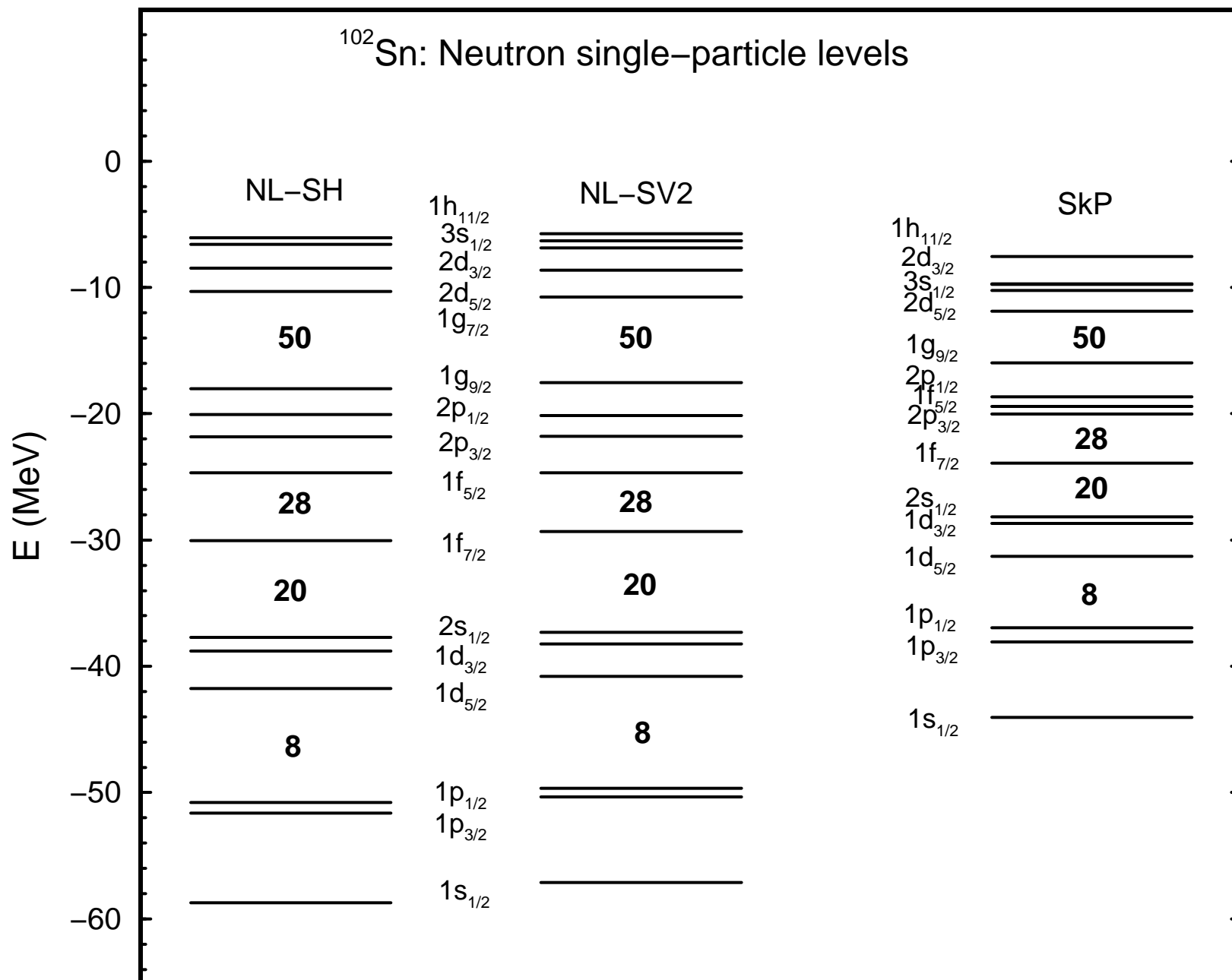


Fig. 16

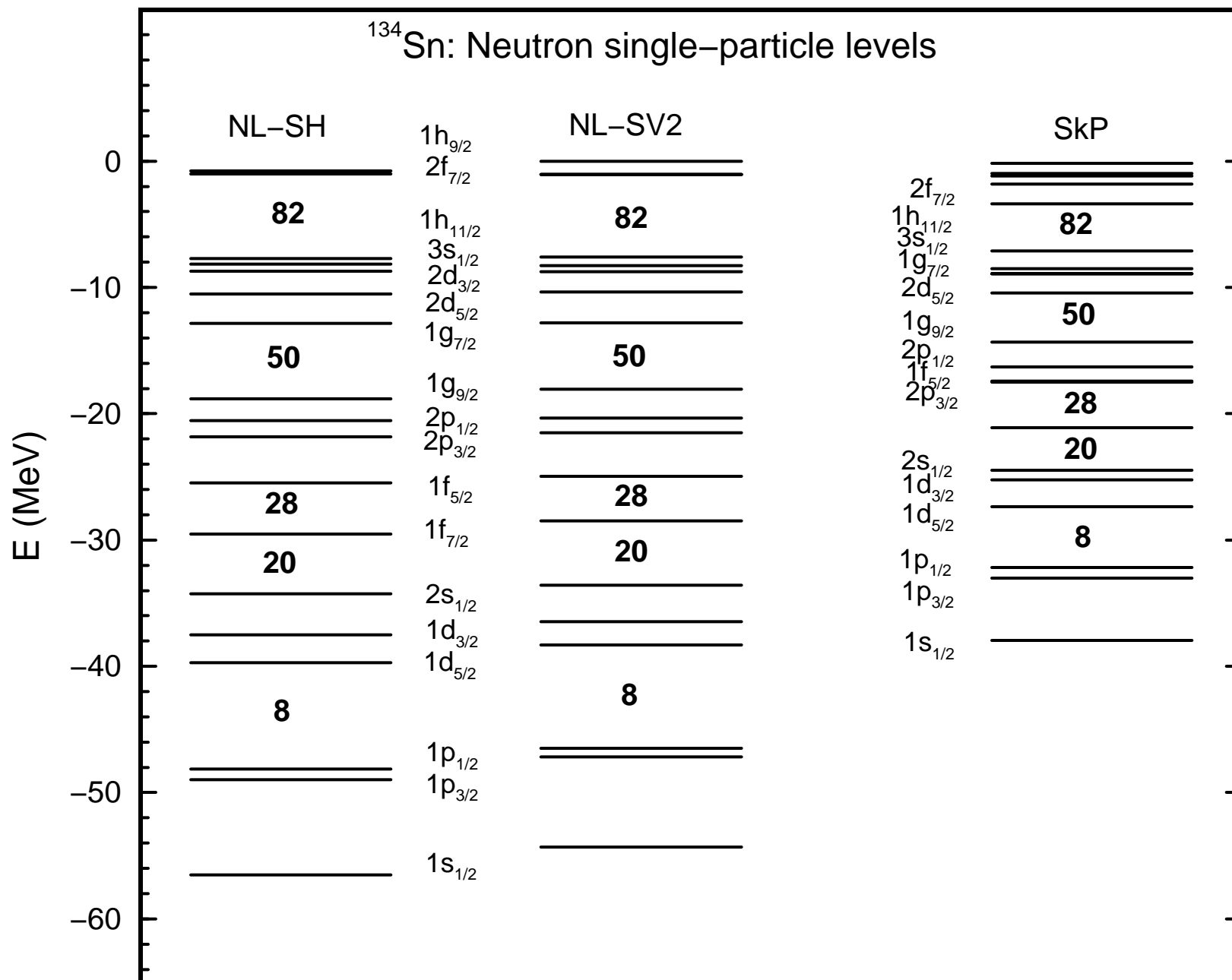


Fig. 17

Fig. 18

